Chapter 3 (Part I)

Bismuth oxide (Bi_2O_3): A promising electrode material for Al^{3+} ion storage

Nandi, S., and Das, S. K. *Solid State Ionics*, 347:115228, 2020.

Bismuth oxide (Bi_2O_3): A promising electrode material for Al^{3+} ion storage

3.1.1 Introduction

In the previous two chapters, the electrochemistry of Al^{3+} ion insertion in graphite in aqueous electrolyte was discussed. It was noticed that electrochemical exfoliation of graphite followed by thermal treatment is an important step to enhance the Al^{3+} ion storage capacity. This chapter discusses the Al^{3+} ion storage capability of bismuth oxide (Bi_2O_3) in aqueous electrolyte. Bismuth oxide (Bi_2O_3) is an emerging electrode material, which has been investigated for non-aqueous Li-ion batteries, Na-ion batteries and supercapacitors [1-10]. The Li^+ ion storage behavior of Bi_2O_3 was investigated by Fiordiponti et al. almost four decades ago [2]. It was recently followed by a study by Li et al., where Li^+ ion discharge capacity of 782 $mAhg^{-1}$ was shown over 40 cycles at a current rate of 100 mAg^{-1} [3]. Similarly, Nithya et al. demonstrated the Na^+ ion storage capability of Bi_2O_3 with discharge capacity of 669 $mAhg^{-1}$ over 200 cycles at a current rate of 350 mAg^{-1} [4]. Again, Li et al. demonstrated the performance of a Ni/Bi battery with Bi_2O_3 nanoflake as anode which delivers specific capacity of 110 $mAhg^{-1}$ at a current rate of 2 Ag^{-1} [5]. Very recently, Zuo et al. reported the electrochemical behavior of Bi_2O_3 in certain monovalent (Li^+, Na^+, K^+) and divalent (Mg^{2+}, Ca^{2+}, Sr^{2+}, Ba^{2+}) ion conducting aqueous electrolytes [11]. However, there are no detailed studies on electrochemical Al^{3+} ion insertion/extraction in Bi_2O_3 in aqueous electrolytes. Although, Zuo et al. touched upon the electroactivity of Al^{3+} ion in Bi_2O_3, there are very limited details. For example, there is complete loss of information of the cathodic redox peak due to the interference from H_2 evolution and the long-term cycling stability of Bi_2O_3 is also unknown. It is shown in this chapter the distinct electrochemical redox activities and long-term cycling stability of Bi_2O_3 in Al^{3+} ion conducting aqueous electrolyte. When assembled with an Al anode, Bi_2O_3 delivers a stable specific capacity of 103 $mAhg^{-1}$ at a current rate of 1.5 Ag^{-1} over several cycles. It is also demonstrated that an integrated approach of tethering Bi_2O_3 particles to an exfoliated graphite current collector is required for mitigating the sharp decline in the storage capacity of Bi_2O_3 in aqueous electrolyte.

3.1.2 Experimental Section

3.1.2.1 Materials

Bismuth (III) nitrate pentahydrate [$Bi(NO_3)_3.5H_2O$, Merck], Acetone, Ethylene glycol [$C_2H_6O_2$, Merck] and Distilled water.

3.1.2.2 Synthesis

Synthesis of Bi_2O_3: Pristine Bi_2O_3 was synthesized by a simple solvothermal process [11]. Briefly to describe, 0.6 g of bismuth (III) nitrate pentahydrate is dissolved in a mixture of ethylene glycol (6 ml) and acetone (12 ml). The mixture was poured in a Teflon autoclave and heated at 160 ^oC for 5 h. The brown product was recovered by centrifugation after washing with water/ethanol and dried at 100 ^oC for 12 h. The washing of the as synthesized Bi_2O_3 sample with water/ethanol was necessary to flush out any residual ethylene glycol from the sample. The harvested Bi_2O_3 sample after centrifugation was thoroughly dried to evaporate any solvent from the sample so that the accurate measurement of the mass of Bi_2O_3 could be done and a slurry could be prepared by mixing Bi_2O_3 and polyvinylidene fluoride (PVDF) in N-methyl-2-pyrrolidone.

Synthesis of integrated Bi_2O_3: For the preparation of an integrated electrode of Bi_2O_3, an already exfoliated graphite foil was immersed in the above mixture and performed the solvothermal treatment as described above. The integrated Bi_2O_3 electrode was collected after the heat treatment and flushed with water/ethanol and dried at 110 ^oC for 12 h. Preparation of exfoliated graphite was already discussed in the previous two chapters.

3.1.2.3 Characterization

The crystallographic phase identification was performed by using powder X-ray diffraction (BRUKER AXS D8 FOCUS; Cu-K_α radiation, λ = 1.5406 Å). The morphology was observed by scanning electron microscopy (SEM, JEOL JSM 6390LV) and transmission electron microscopy (TEM, JOEL JEM 2100). Quantification of specific surface areas (BET) of pristine graphite and exfoliated graphite was done from N_2 adsorption-desorption isotherms (Quantachrome, NOVA 1000E). For this purpose, the entire exfoliated portion of the exfoliated graphite electrode (positive '+' electrode of Figure 3.1.4) was used for the measurement.

3.1.2.4 Electrochemical analysis

Electrode slurry was made from Bi_2O_3, polyvinylidene fluoride and N-methyl-2-pyrrolidone. The weight ratio of Bi_2O_3 and polyvinylidene fluoride is 80:20. This slurry was cast on pristine graphite foil and exfoliated graphite foil and both of them are dried at 110 ^oC for 12 h. Hence, three different types of electrodes were obtained. These were Bi_2O_3 on pristine graphite, Bi_2O_3 on exfoliated graphite and an integrated electrode of Bi_2O_3 on exfoliated graphite. These electrodes are respectively abbreviated as Bi_2O_3/Gr, Bi_2O_3/Exf. Gr and Int. Bi_2O_3/Exf. Gr. The active masses (Bi_2O_3) present in both Bi_2O_3/Gr and Bi_2O_3/Exf. Gr are estimated by subtracting the mass of the pristine graphite or exfoliated graphite current collector from the electrode slurry coated graphite or exfoliated graphite working electrode. The mass loading was in the range of 1.5-2.5 $mgcm^{-2}$.

Cyclic voltammetry (CV) and galvanostatic discharge/charge experiments were performed in a conventional three-electrode electrochemical glass cell. Pt electrode and aqueous Ag/AgCl electrode were used as the counter and reference electrodes respectively while Bi_2O_3/Gr, Bi_2O_3/Exf. Gr and Int. Bi_2O_3/Exf. Gr act as the working electrode. The utilized electrolyte was 1 M $AlCl_3.6H_2O$ aqueous solution. It is noted here that $AlCl_3.6H_2O$ is a highly water-soluble salt. The dissociation of $AlCl_3.6H_2O$ in water had already been investigated using Raman spectroscopic technique and it indicates the formation of hydrated Al^{3+} cation and Cl^- anion in the electrolyte [12]. The discharge/charge and CV experiments were performed in the voltage range of -0.8 V to 0.3 V and -1 V to 0.3 V respectively. Electrochemical impedance spectra were obtained by scanning in the frequency range of 1 mHz-200 kHz at signal amplitude of 10 mV. The working electrode was connected to Bi_2O_3/Gr, Bi_2O_3/Exf. Gr and Int. Bi_2O_3/Exf. Gr electrodes for this purpose.

An aqueous Al-cell was tested with Al metal as anode and Bi_2O_3 as cathode. Typically used Al foil (Hindalco Freshwrapp) for household purposes was utilized for this purpose. The utilized electrolyte was 1 M $AlCl_3.6H_2O$ aqueous solution. The galvanostatic discharge/charge and CV experiments were performed in the voltage range of 0-1.2 V considering Bi_2O_3/Gr, Bi_2O_3/Exf. Gr and Int. Bi_2O_3/Exf. Gr electrodes as the working electrode and Al as both the reference and counter electrodes. For ex-situ XRD and SEM experiments, the electrodes were harvested

after required number of discharge/charge cycles and dried at 110 ^{o}C for 24 h. All the electrochemical experiments were conducted at room temperature (25 ^{o}C) and at ambient atmosphere.

3.1.3 Results and Discussion

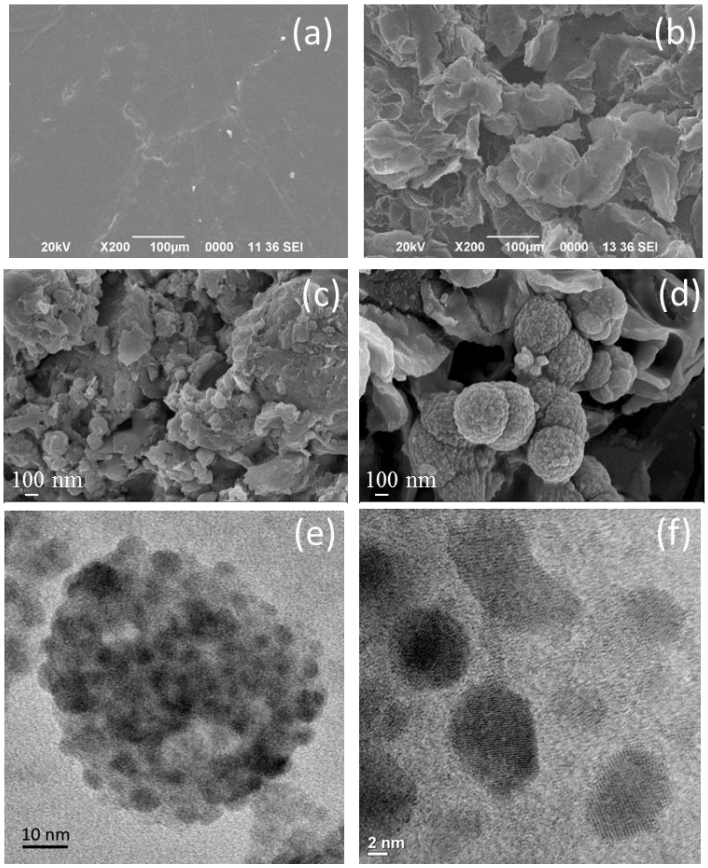

Figure 3.1.1 SEM images of (a) pristine graphite foil, (b) exfoliated graphite foil, (c) pristine Bi_2O_3 particles and (d) Int. Bi_2O_3/Exf. Gr. (e, f) TEM images of Bi_2O_3 particles extracted from Int. Bi_2O_3/Exf. Gr electrode.

Figure 3.1.1 (a, b) shows the SEM images of pristine graphite and electrochemically exfoliated graphite. The surface of the exfoliated graphite is covered with nanoflakes (Figure 3.1.1b). The XRD patterns are also shown in Figure 3.1.2. The exfoliated graphite retains the graphitic structure; however, the diffraction peak (002) is broadened by an amount of 0.023^{o} suggesting formation of nanoflakes on the surface of exfoliated graphite. N_2 adsorption/desorption isotherms (Figure 3.1.3) indicate the existence of mesopores for EG and very little micropores in pristine graphite-based adsorbents. The BET surface area of the exfoliated graphite (39 m^2g^{-1}) is higher than the pristine graphite (29 m^2g^{-1}). The electrochemical

exfoliation of graphite to obtain graphene nanosheets is a known process [13-16]. Several research groups explored this technique in aqueous and ionic liquid electrolytes containing various inorganic salts such as $(NH_4)_2SO_4$, Na_2SO_4, K_2SO_4 [13-16]. We used $AlCl_3$ aqueous solution for this process for the first time. It is noted here that graphite electrode on the positive terminal exhibits the maximum exfoliation as shown in Figure 3.1.4c. This may be explained based on the proposed model by Parvez et al. [14-15]. Initially, the water molecules oxidize to hydroxyl (OH·) and oxygen (O·) radicals under the influence of the applied electric field. These radicals react with the C atoms at the interface of electrolyte and graphite electrode. It thus results in the opening of the graphitic layers near the edges. Consequently, the Cl^- anions are prompted to intercalate between the graphitic layers since the graphite electrode is maintained at positive potential. There are evidences of Cl^- anion intercalation in graphite in the literature [17-18]. The intercalated Cl^- anions further result in the formation of Cl_2 gas ($2Cl^- \rightarrow Cl_2 + 2e^-$). It is expected that these gas molecules exfoliate the graphite electrode while escaping from the graphitic layers.

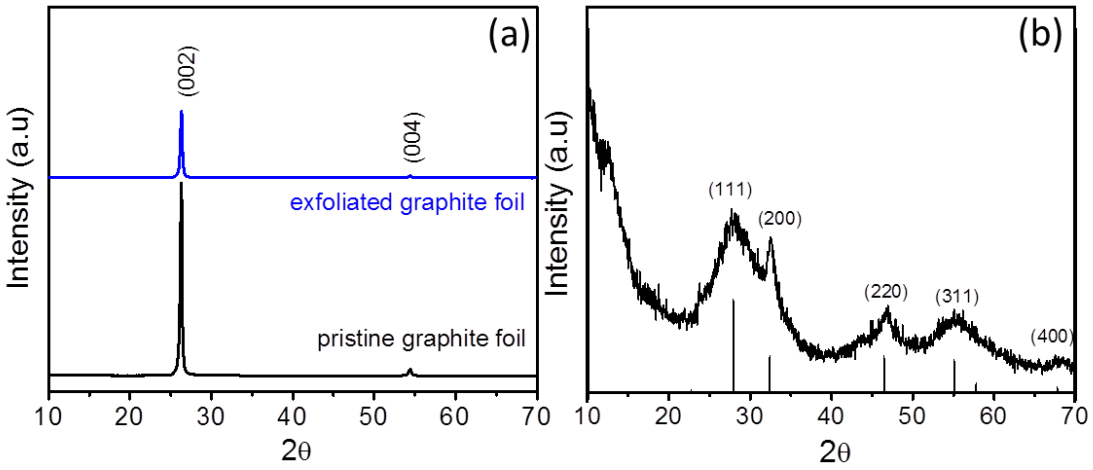

Figure 3.1.2 XRD patterns for (a) pristine graphite/exfoliated graphite foil and (b) pristine Bi_2O_3 particles. The vertical bars are from δ-Bi_2O_3 phase with JCPDS 27-0052.

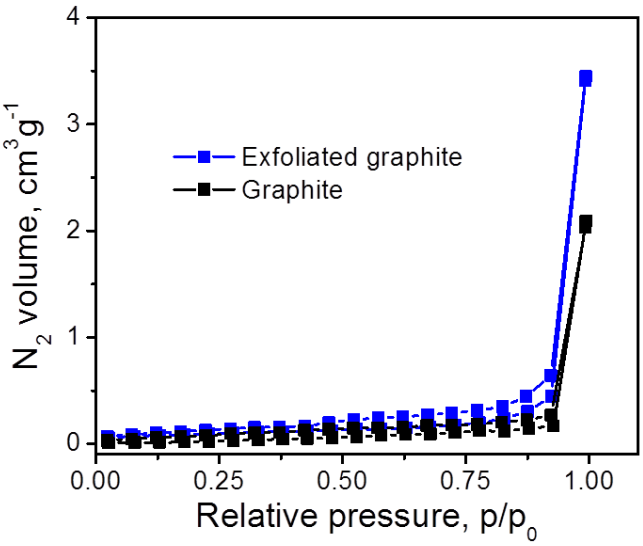

Figure 3.1.3 N_2 adsorption/desorption isotherms of pristine graphite foil and exfoliated graphite foil.

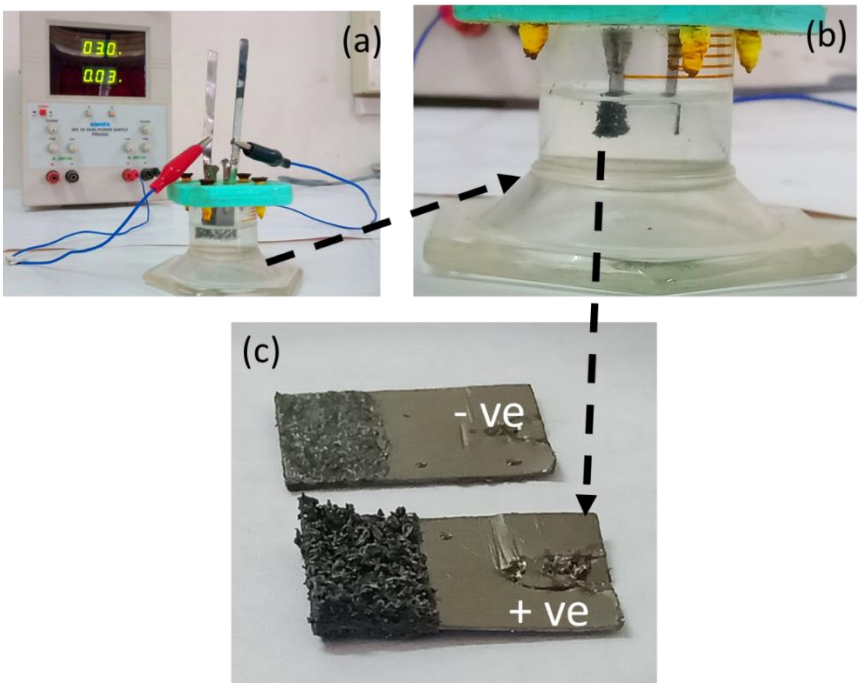

Figure 3.1.4 (a) Experimental set up for performing the electrochemical exfoliation of graphite, (b) The enlarged view of the exfoliated graphite region for better clarity and (c) photograph of graphite foils after exfoliation.

The XRD pattern (Figure 3.1.2b) indicates that the synthesized Bi_2O_3 is crystallized in the δ-phase of Bi_2O_3 (JCPDS 27-0052) with a space group *Pm*3*m*. The broadening of diffraction peaks may be attributed to the formation of nanosized crystallites of Bi_2O_3 as evidenced from the SEM image (Figure 3.1.1c). The XRD pattern of Int. Bi_2O_3/Exf. Gr (Figure 3.1.5) also indicates δ-phase of Bi_2O_3. The peaks

are not so prominently visible due to the large intensity diffraction peak from graphite substrate and small amount of Bi_2O_3 deposition (typically 1-2 mg cm^{-2}) on the substrate. However, as could be seen in Figure 3.1.1c and Figure 3.1.5c, a considerable difference in the morphology of the Bi_2O_3 particles in Int. Bi_2O_3/Exf. Gr is observed. Contrary to random shaped particles in pristine Bi_2O_3, spherical particles of various dimensions in the range of 100 nm to 5 µm could be noticed in Int. Bi_2O_3/Exf. Gr (Figure 3.1.5c). TEM image (3.1.1e) of these large Bi_2O_3 spherical particles indicate that they are composed of aggregates of small Bi_2O_3 nanoparticles of size 5-10 nm (Figure 3.1.1f).

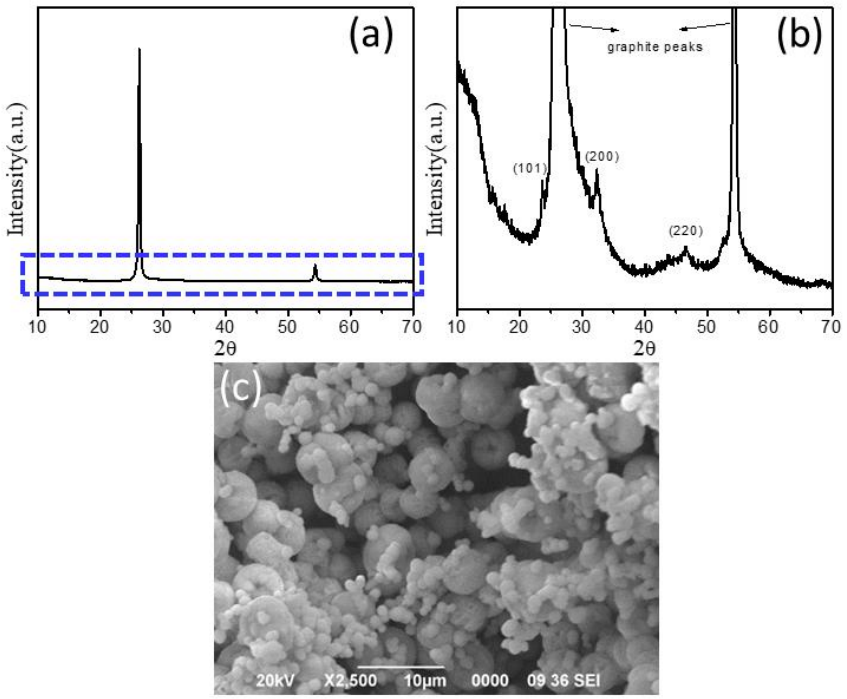

Figure 3.1.5 XRD pattern of (a) Int. Bi_2O_3/Exf. Gr electrode and (b) enlarged view of the dotted blue region for better clarity. (c) SEM image of Int. Bi_2O_3/Exf. Gr.

Initially, cyclic voltammetry (CV) experiments were carried out in a conventional three electrode electrochemical system to verify any Al^{3+} ion electrochemical activity in Bi_2O_3. For this purpose, the utilized electrolyte is an aqueous solution of 1 M $AlCl_3$. Figure 3.1.6a shows the CV profile of Bi_2O_3/Gr at a scan rate of 2.5 mVs^{-1}. It clearly indicates considerable electroactivity of Bi_2O_3. Two cathodic peaks, designated as A and B in the Figure 3.1.6a, could be seen at -0.3 V and -0.70 V respectively in the initial cathodic scan. However, only one prominent anodic peak at -0.03 V (peak C) appears in all the anodic scans and the peak intensities of both the cathodic and anodic peaks gradually decline with increasing

cycle number indicating decreasing electrochemical activity. The Al^{3+} ion electrochemical activity is also observed for Bi_2O_3/Exf. Gr and Int. Bi_2O_3/Exf. Gr (Figure 3.1.6b and 3.1.6c respectively). While the redox peaks A, B and C are almost located at the identical potential positions in these two electrodes, there is a noticeable difference in the current densities in these two cases in comparison to Bi_2O_3/Gr. The increasing order of current densities in these electrodes is as follows: Bi_2O_3/Gr < Bi_2O_3/Exf. Gr < Int. Bi_2O_3/Exf. Gr. The enhanced current density suggests improved electroactivity of Bi_2O_3 in Int. Bi_2O_3/Exf. Gr. The appearance of two prominent cathodic peaks in all of the cases is in stark contrast to the report of Zuo et al., where only the anodic peak was detected [11]. It is noted that neither graphite nor the exfoliated graphite current collector exhibits any electrochemical activity in the measured potential range of Bi_2O_3 as shown in the CV profiles (Figure 3.1.7).

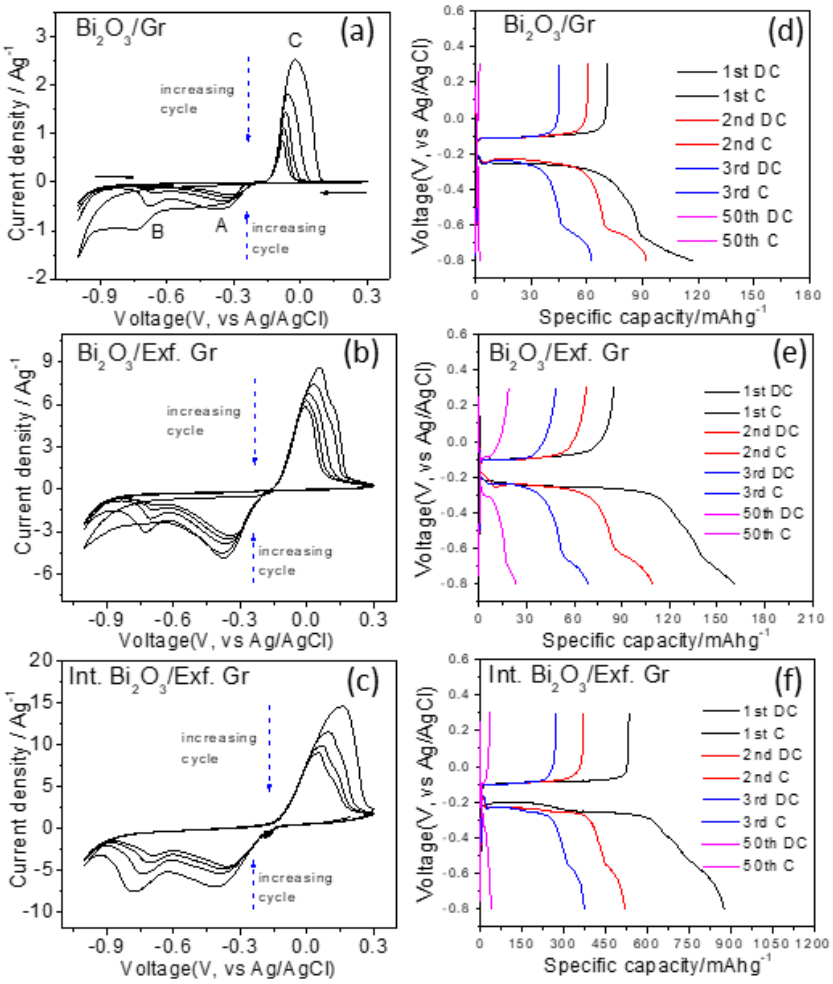

Figure 3.1.6 CV curves of (a) Bi_2O_3/Gr, (b) Bi_2O_3/Exf. Gr, (c) Int. Bi_2O_3/Exf. Gr at a scan rate of 2.5 mVs^{-1}; Galvanostatic discharge/charge curves of (d) Bi_2O_3/Gr, (e) Bi_2O_3/ Exf. Gr and (f) Int. Bi_2O_3/Exf. Gr at a current density of 1.5 Ag^{-1}.

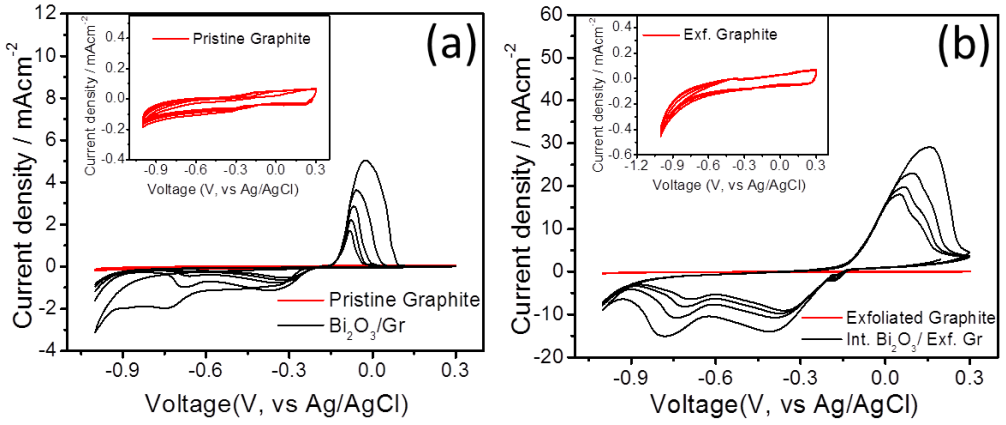

Figure 3.1.7 CV profiles of (a) pristine graphite and (b) exfoliated graphite in 1 M $AlCl_3$ aqueous electrolyte at a scan rate of 2.5 mVs^{-1}.

In order to evaluate the Al^{3+} ion storage capacities of Bi_2O_3, galvanostatic discharge/charge experiments were conducted. The discharge/charge profiles of Bi_2O_3/Gr in 1 M $AlCl_3$ aqueous electrolyte in the voltage range of -0.8 V to 0.3 V (vs. Ag/AgCl) at a current rate of 1.5 Ag^{-1} is shown in Figure 3.1.6d. These profiles exhibit clear flat charge/discharge plateaus. There exists one distinct long discharge potential plateau at -0.24 V and a kink at -0.6 V during discharge cycles. On the other hand, the charging potential plateau is at -0.1 V. These features are fairly in corroboration with the CV profiles (Figure 3.1.6a). The initial discharge and charge capacities are 117.5 $mAhg^{-1}$ and 71.1 $mAhg^{-1}$ respectively. Similar to the CV profiles, there is a gradual decline in the specific capacities with increasing cycle numbers (Figure 3.1.6d and Figure 3.1.8). The specific capacities almost reach zero after 20^{th} cycle. The flat charge/discharge potential plateaus could also be noticed for Bi_2O_3/Exf. Gr and Int. Bi_2O_3/Exf. Gr at almost identical potential positions (Figure 3.1.6e and 3.1.6f). Interestingly, there is an improvement in the specific capacities. In case of Bi_2O_3/Exf. Gr, the discharge and charge capacities are 161.3 $mAhg^{-1}$ and 84.5 $mAhg^{-1}$ respectively in the 1^{st} cycle. The discharge capacity value maintains at 20 $mAhg^{-1}$ at 100^{th} cycle (Figure 3.1.8). On the other hand, the initial specific capacities are significantly high for Int. Bi_2O_3/Exf. Gr in comparison to Bi_2O_3/Gr and Bi_2O_3/Exf. Gr. The respective initial discharge and charge capacities are 875 $mAhg^{-1}$ and 534 $mAhg^{-1}$. There is also an improvement in the cycling stability with stable specific capacity values of 30 $mAhg^{-1}$ at 100^{th} cycle (Figure 3.1.8). The current rate was identical in all the three cases. This improvement is expected to be due to the better

contact of Bi_2O_3 particles in the exfoliated graphene nanoflakes. The SEM images of the electrodes hint at it. The Bi_2O_3 particles are uniformly distributed in the exfoliated graphite current collector in case of Int. Bi_2O_3/Exf. Gr (Figure 3.1.9b), but exposed areas of current collector could be noticed for Bi_2O_3/Exf. Gr (Figure 3.1.9a). The intimate contact of Bi_2O_3 in the exfoliated graphite current collector consequently manifests in lowering the interfacial charge transfer resistance. It is well evidenced from the electrochemical impedance spectroscopy investigation. The comparison of the charge transfer resistances, as shown in Figure 3.1.9c, indicates much lower contact resistance for Int. Bi_2O_3/Exf. Gr. In fact, the increasing order of this resistance is as follows: Int. Bi_2O_3/Exf. Gr. (1992 Ωm^{-2}) < Bi_2O_3/Exf. Gr (19449 Ωm^{-2}) < Bi_2O_3/Gr (20388 Ωm^{-2}). This is very much consistent with the electrochemical stability data.

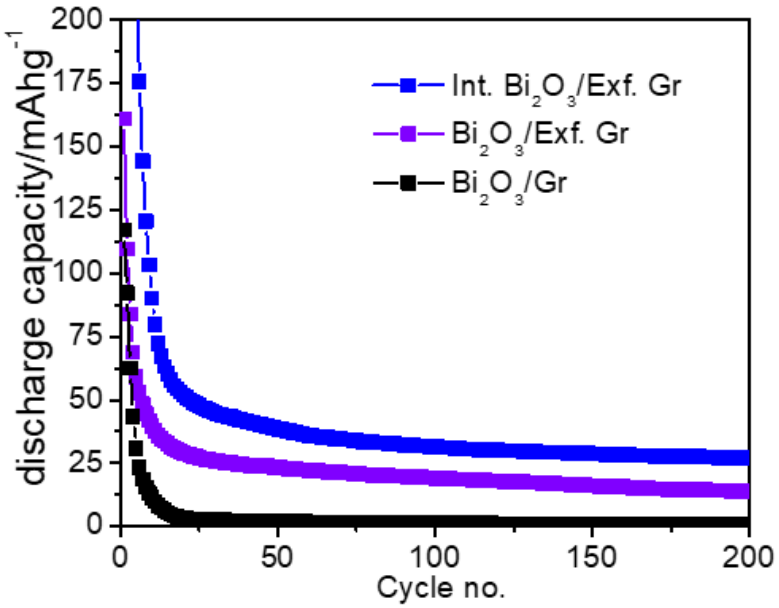

Figure 3.1.8 Variation of discharge capacities with cycle number at a specific current of 1.5 Ag^{-1}.

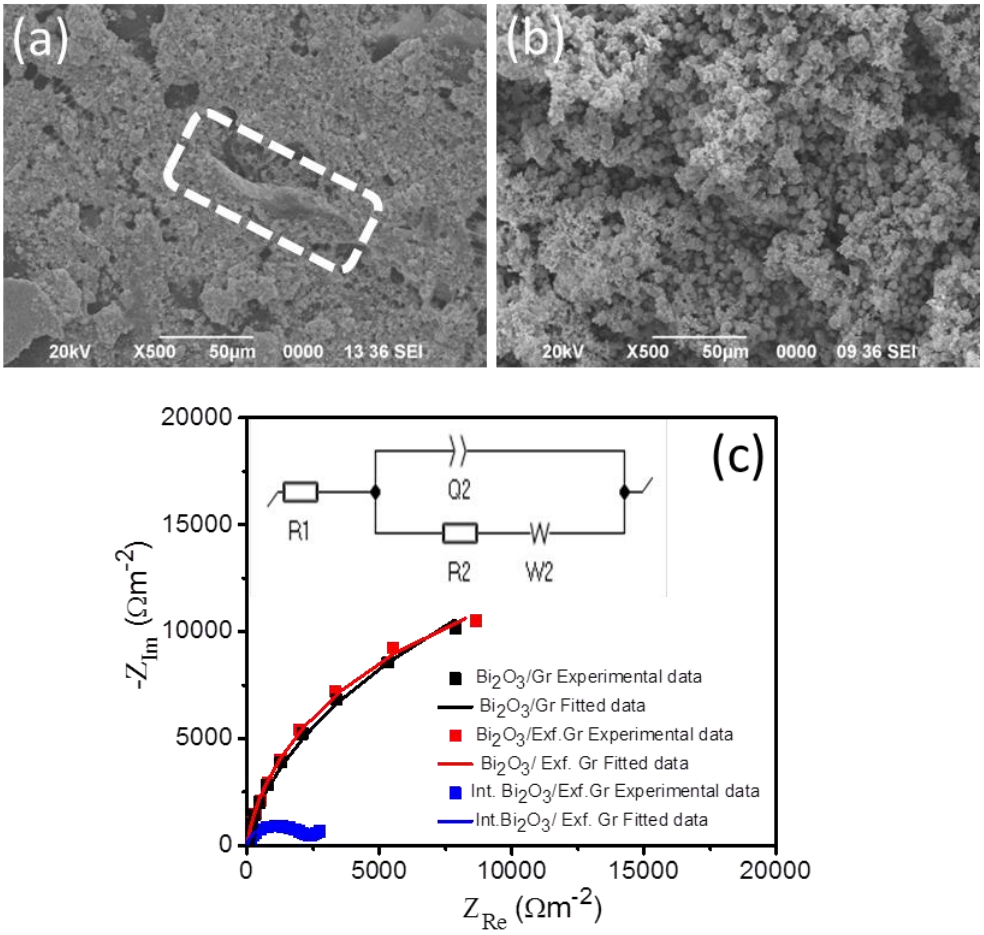

Figure 3.1.9 SEM images of (a) Bi_2O_3/Exf. Gr and (b) Int. Bi_2O_3/Exf. Gr. The dotted region shows the exposed area of the current collector, (c) Electrochemical impedance spectra for Bi_2O_3/Gr, Bi_2O_3/Exf. Gr and Int. Bi_2O_3/Exf. Gr. Inset of Figure 3.1.9c shows the equivalent circuit used for fitting the impedance spectra. R2 represents the R_{ct} value.

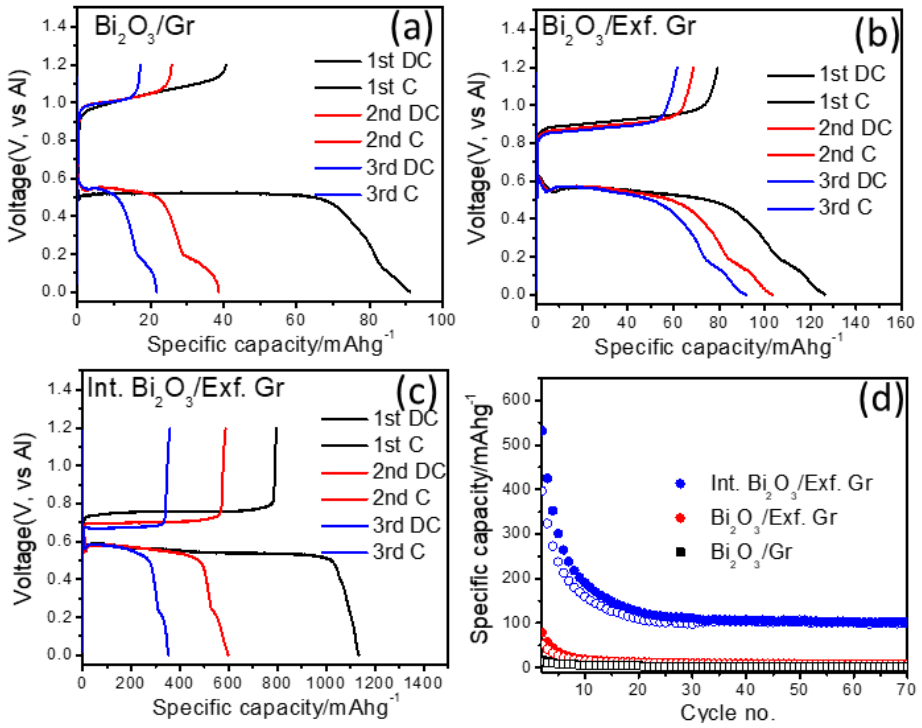

Figure 3.1.10 Galvanostatic discharge/charge curves of full-cell (aqueous Al-ion) with (a) Bi_2O_3/Gr, (b) Bi_2O_3/Exf. Gr and (c) Int. Bi_2O_3/Exf. Gr at a current density of 0.5 Ag^{-1} and (d) Variation of discharge/charge capacities with cycle number at a specific current of 1.5 Ag^{-1}.

The electrochemical activity of Bi_2O_3 is again investigated in a full-cell aqueous Al-metal battery in 1 M $AlCl_3$ aqueous electrolyte. The full-cell consists of Al metal and Bi_2O_3 as electrodes. All the investigated Al-Bi_2O_3 cell demonstrate good reversibility with varying degree of specific capacities. Figure 3.1.10 (a-c) shows the respective charge/discharge profiles at a current rate of 0.5 Ag^{-1}. The cells show a long discharge potential plateau at 0.55 V (vs Al). However, the charging potential plateaus are slightly at different potential positions. These are at 1 V, 0.9 V and 0.7 V for Al-Bi_2O_3/Gr, Al-Bi_2O_3/Exf. Gr and Al-Int. Bi_2O_3/Exf. Gr cells respectively. Apart from it, there is a significant jump in the discharge/charge capacities for Al-Int. Bi_2O_3/Exf. Gr cell in comparison to Al-Bi_2O_3/Gr and Al-Bi_2O_3/Exf. Gr cells. The respective initial discharge and charge capacities are 1130 $mAhg^{-1}$ and 798 $mAhg^{-1}$ for Al-Int. Bi_2O_3/Exf. Gr cell (Figure 3.1.10c). These values are only 126 $mAhg^{-1}$ and 78 $mAhg^{-1}$ for Al-Bi_2O_3/Exf. Gr cell (Figure 3.1.10b), and 91 $mAhg^{-1}$ and 40 $mAhg^{-1}$ for Al-Bi_2O_3/Gr cell (Figure 3.1.10a). The variation of specific capacities with cycle number at current rate of 1.5 Ag^{-1} is shown in Figure 3.1.10d. As could be seen, there

is a gradual decline of specific capacities in all cases. The worst performance is shown by Al-Bi_2O_3/Gr cell with discharge capacity values close to zero after 5th cycle followed by Al-Bi_2O_3/Exf. Gr cell with a value of only 8 $mAhg^{-1}$ at the 50th cycle. On the other hand, much improved stability and enhancement in specific capacities of Al-Int. Bi_2O_3/Exf. Gr cell could be noticed (Figure 3.1.10d). The discharge capacity is significantly high and it is 103 $mAhg^{-1}$ at the 50th cycle. It is worth here to mention the contribution of exfoliated graphite current collector in estimating the overall capacity of Bi_2O_3. To ascertain it, galvanostatic discharge/charge experiment was performed with pristine exfoliated graphite (i.e. with no Bi_2O_3 on it) as a working electrode in 1 M $AlCl_3$ aqueous electrolyte. Figure 3.1.11 shows the comparison of discharge/charge profiles of pristine exfoliated graphite and Int. Bi_2O_3/Exf. Gr at a current density of 1 $mAcm^{-2}$. In this case, the storage capacities (i.e. areal capacity) are normalized with respect to the area of the working electrodes since there involves no active material (Bi_2O_3) [19]. It is clearly evident that the exfoliated graphite electrode shows negligible storage capacity in the measured voltage range (Figure 3.1.11). Hence, it could be commented that the storage capacities observed with Int. Bi_2O_3/Exf. Gr is entirely due to Bi_2O_3 and not because of the exfoliated graphite current collector. Hence, the improvement is again could be attributed to the reduced charge transfer resistance between the electrode material (Bi_2O_3) and the current collector (exfoliated graphite) in case of Int. Bi_2O_3/Exf. Gr. It is appropriate here to mention about the utilization of Al metal in aqueous electrolyte. Recently, the rechargeability of Al metal in aqueous electrolyte is demonstrated by Zhao et al. [20]. They adopted an approach of creating artificial solid electrolyte interphase at the surface of Al metal, which facilitates the reversible stripping and plating of Al in aqueous $Al(CF_3SO_3)_3$ electrolytes. The CV profile of Al-Int. Bi_2O_3/Exf. Gr cell is shown in Figure 3.1.13a. One pair of major cathodic and anodic redox peaks could be observed at 0.45 V and 0.88V (vs Al) respectively in all the scans signifying good electrochemical reversibility which is fairly in corroboration with the discharge/charge profiles.

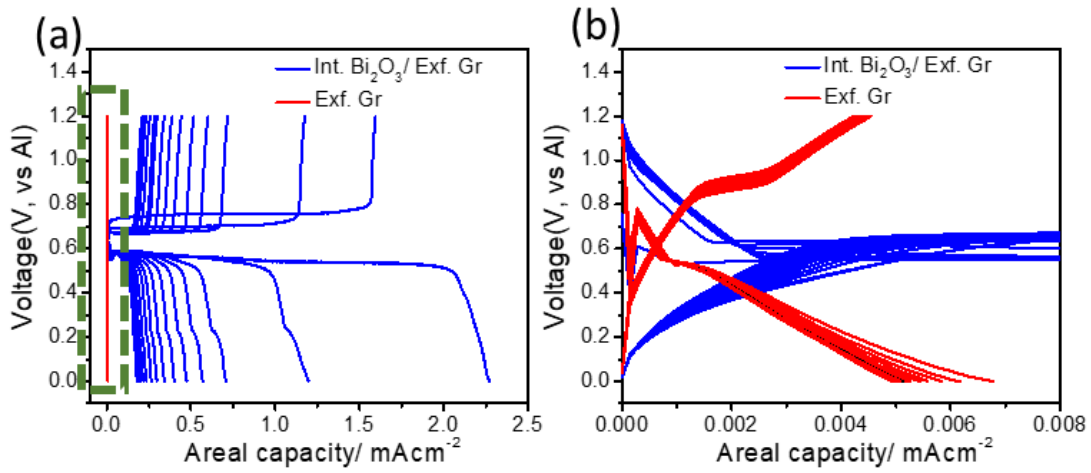

Figure 3.1.11 (a) Comparison of galvanostatic discharge/charge profiles of pristine exfoliated graphite and Int. Bi_2O_3/Exf. Gr at a current density of 1mAcm^{-2}. (b) Enlarged view of the green dotted box to show the charge/discharge profiles of pristine exfoliated graphite.

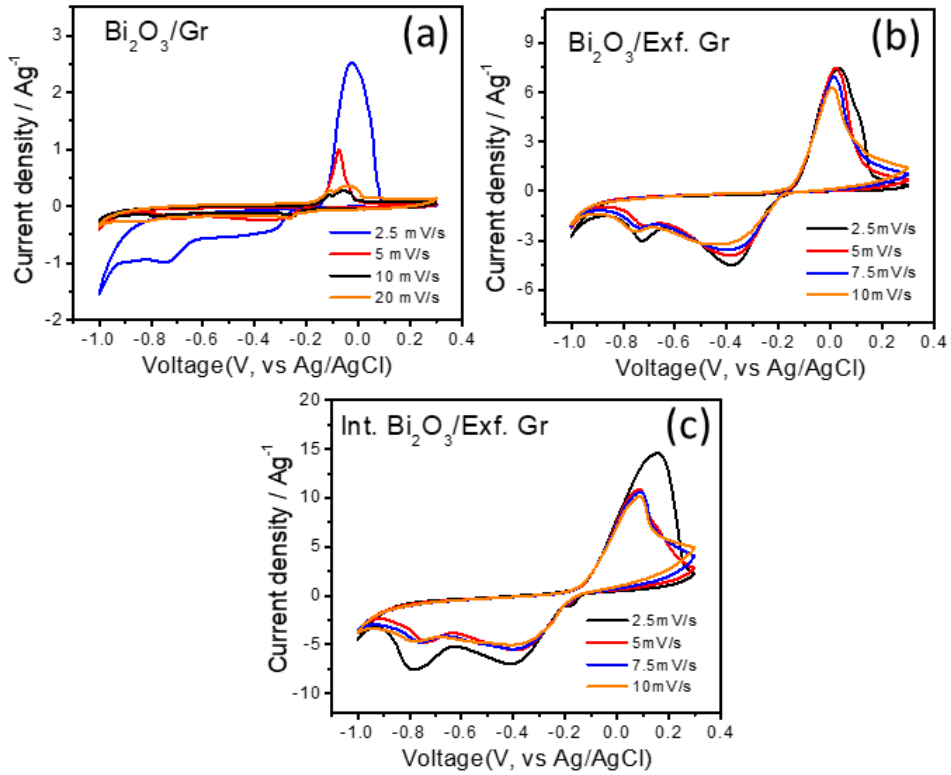

Figure 3.1.12 CV profiles of (a) Bi_2O_3/Gr, (b) Bi_2O_3/Exf. Gr and (c) Int. Bi_2O_3/Exf. Gr at various scan rates in three electrode set-up.

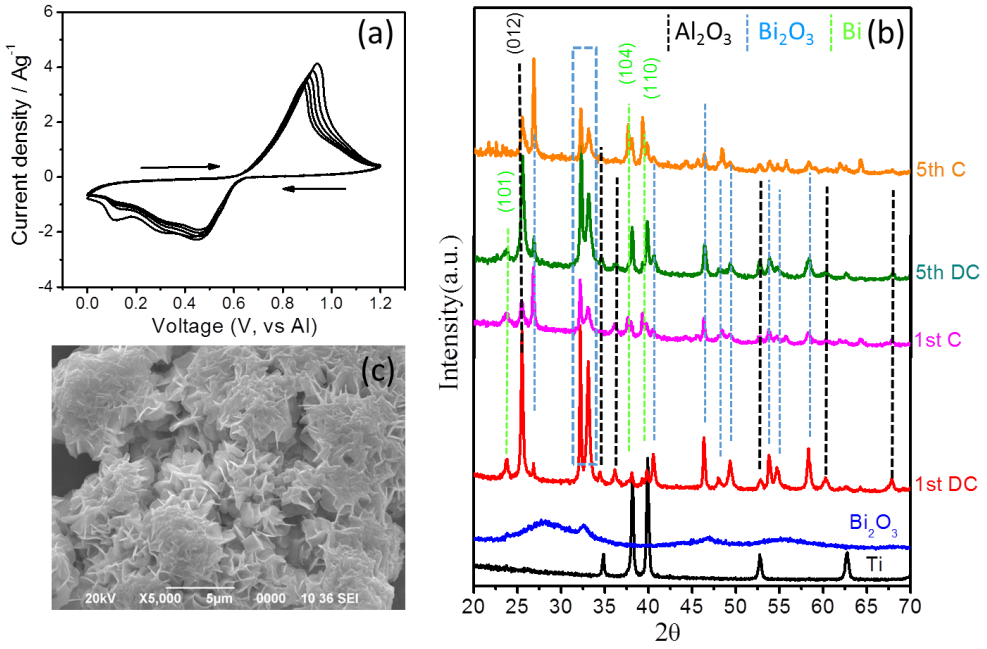

Figure 3.1.13 CV profile of Al-Int. Bi_2O_3/Exf. Gr cell at a scan rate of 5 mVs^{-1}, (b) Ex-situ XRD patterns of Bi_2O_3 electrode before discharge, after discharge ($1^{st}/5^{th}$) and charge ($1^{st}/5^{th}$), (c) Ex-situ SEM image of Int. Bi_2O_3/Exf. Gr after 1^{st} discharge.

The CV profiles of Bi_2O_3 at different scan rates are shown in Figure 3.1.12. It is noticed that the peak current responses (I) for both the cathodic and anodic redox peaks do not follow any relationship with scan rates (γ) according to the equation $I = k\gamma^{0.5}$ (k is a constant), which rules out the possibility of non-diffusive process [21]. Ex-situ XRD measurement was performed with discharged and charge state electrodes. For this particular purpose, Ti was used as the current collector to avoid the intense (002) peak from graphite current collector. Figure 3.1.13b shows the ex-situ XRD patterns. The discharge/charge XRD patterns are completely different from the parent Bi_2O_3 with emergence of several sharp diffraction peaks. It is noticed that fairly a large number of additional diffraction peaks emerge after 1^{st} discharge. It is also noted here that the diffraction patterns are very complex in nature and it appears that the diffraction peaks are overlapping with various possible crystallographic phases of Al_2O_3, Bi_2O_3, Bi as shown in Figure 3.1.14. In addition, there are large numbers of diffraction peaks from unknown crystallographic phases. The presence of such several known and unknown crystal phases is a clear manifestation of very complex electrochemical processes involved while Al^{3+} ions electrochemically react with Bi_2O_3 in aqueous electrolytes. The crystallographic phases were identified from

these XRD patterns (Figure 3.1.13b and Figure 3.1.14). One of the major peaks is at $2\theta = 25.49^{o}$. The intensity of this peak reduces drastically after subsequent charging. Even after 5^{th} discharge/5^{th} charge cycle, this peak could be seen with the same pattern of emergence and disappearance. This diffraction peak could be identified as one of the most intense peaks from Al_2O_3 (JCPDS-42-1468, JCPDS-42-1212). Other diffraction peaks from Al_2O_3 phase are identified at $2\theta = 34.49^{o}$ and $2\theta = 36.15^{o}$. Similarly, diffraction peaks positioned at $2\theta = 26.82^{o}$ and $2\theta = 33.07^{o}$ are exactly matching with Bi_2O_3 (JCPDS-41-1449). The Bi_2O_3 diffraction peak at $2\theta = 46.28^{o}$ overlaps with Al_2O_3 phase (JCPDS-16-0394). The intense diffraction peak due to Bi also almost overlaps with the Bi_2O_3 peak around $2\theta = 26.82^{o}$ (JCPDS-44-1246). Other two identified intense Bi peaks are at $2\theta = 37.98^{o}$ and $2\theta = 39.29^{o}$. One of the plausible reasons for the missing diffraction peaks from Al_2O_3 phase is that it may preferentially grow only in one particular crystallographic direction (012). An indirect indication of it could be inferred from the morphological transformation of the spherical Bi_2O_3 particles after discharge as evidenced from the ex-situ SEM images (Figure 3.1.13c and Figure 3.1.15). The discharge state electrodes show structure of nanoflakes, which signifies restricted and preferential growth. Based on it, we comment that it is possible that an electrochemical conversion reaction of the type $Bi_2O_3 + 2Al^{3+} + 6e^{-} \rightarrow 2Bi + Al_2O_3$ occurs during the discharge processes and it is highly reversible. But, the estimated theoretical capacity of Bi_2O_3 according to the proposed reaction is 345 $mAhg^{-1}$, which is lower than the observed maximum discharge capacity (1130 $mAhg^{-1}$). This additional discharge capacity hints at alternative storage mechanisms. Two such plausible mechanisms may be as follows. First, there is a possibility of electrochemical alloying/dealloying reaction between Al and Bi and the unidentified diffraction peaks (Figure 3.1.14b) may arise from Al-Bi alloy phases. This possibility cannot be ruled out since alloying reaction is feasible between Al and Bi [22]. Second, the proposed reaction mechanism leads to the formation of an interface of Bi and Al_2O_3 and, hence, heterogeneous interfacial storage is also a possibility [23-24]. According to this storage concept, Al^{3+} ions can be stored on the Al_2O_3 side of the interface while electrons are localized on Bi side resulting in a charge separation and this interfacial effect is very dominant in nanostructured interfaces [25].

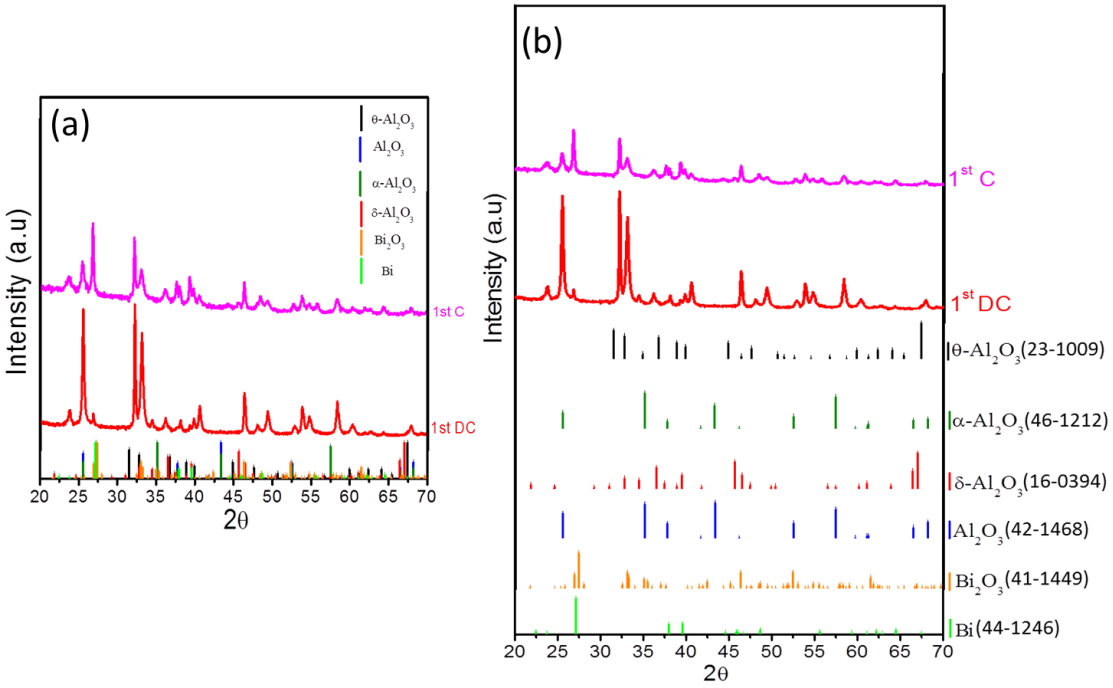

Figure 3.1.14 Ex-situ XRD patterns of Bi_2O_3 electrode after discharge (1^{st}) and charge (1^{st}). (a) JCPDS files are overlapped together and (b) JCPDS files are plotted separately. The relevant JCPDS numbers are given in Figure 3.1.14b.

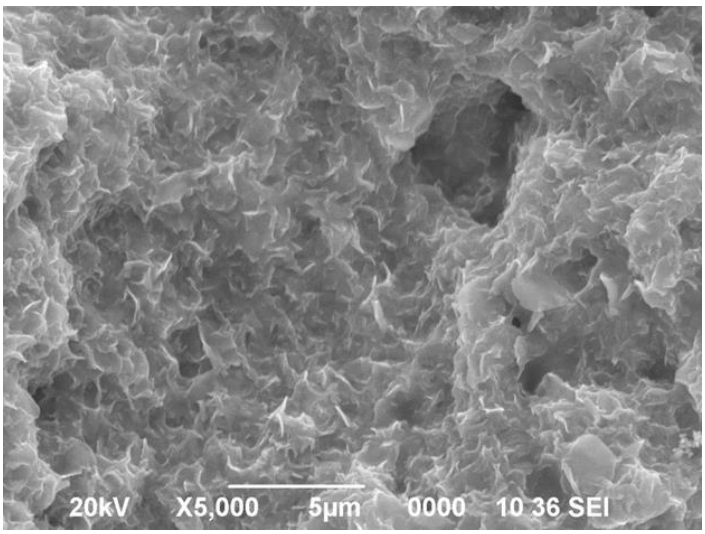

Figure 3.1.15 Ex-situ SEM image of Bi_2O_3/Exf. Gr after 1^{st} discharge.

3.1.4 Conclusion

In summary, this chapter demonstrated the Al^{3+} ion storage in Bi_2O_3 in aqueous electrolyte. While severe specific capacity decline is noticed for pristine Bi_2O_3, there is a scope for simultaneous improvement in long-term cycling stability

and storage capacity by in-situ tethering of Bi_2O_3 particles on an exfoliated graphite current collector. A flat discharge plateau at 0.5 V (vs Al) is obtained with discharge capacity as high as 103 $mAhg^{-1}$ over several cycles with Coulombic efficiency of 99%.

3.1.5 References

[1] Ni J, Bi X, Jiang Y, Li L, and Lu J. Bismuth chalcogenide compounds Bi_2X_3 (X=O, S, Se): applications in electrochemical energy storage. *Nano. Energy,* 34:356-366, 2017.

[2] Fiordiponti P, Pistoia G, and Temperoni C. Behavior of Bi_2O_3 as a cathode for lithium cells. *J. Electrochem. Soc.* 125: 14-17,1978.

[3] Li Y, Trujillo MA, Fu E, Patterson B, Fei L, Xu Y, Deng S, Smirnov S., and Luo H. Bismuth oxide: a new lithium-ion battery anode. *J. Mater. Chem. A*, 1: 12123-12127, 2013.

[4] Nithya C. Bi_2O_3@reduced graphene oxide nanocomposite: an anode material for sodium-ion storage. *ChemPlusChem*, 80:1000-1006, 2015.

[5] Li X, Guan C, Hu Y, and Wang J. Nanoflakes of Ni–Co LDH and Bi_2O_3 assembled in 3D carbon fiber network for high-performance aqueous rechargeable Ni/Bi battery. *ACS Appl. Mater. Interfaces,* 9: 26008-26015, 2017.

[6] Zheng H, Li H, Yu M, Zhang M, Tong Y, Cheng F, and Lu X. Vertical bismuth oxide nanosheets with enhanced crystallinity: promising stable anodes for rechargeable alkaline batteries. *J. Mater. Chem. A* 5: 25539-25544, 2017.

[7] Yin H, Cao M, Yu X, Zhao H, Li C, Shen Y, and Zhu M. Self-standing Bi_2O_3 nanoparticles/carbon nanofiber hybrid films as a binder-free anode for flexible sodium-ion batteries. *Mater. Chem. Front*. 1:1615-1621, 2017.

[8] Zhao J, Li Z, Shen T, Yuan X, Qiu G, Jiang Q, Lin Y, Song G, Meng A, and Li Q. Oxygen-vacancy Bi_2O_3 nanosheet arrays with excellent rate capability and $CoNi_2S_4$ nanoparticles immobilized on N-doped graphene nanotubes as robust electrode materials for high-energy asymmetric supercapacitors. *J. Mater. Chem. A,* 7: 7918-7931, 2019.

[9] Senthilkumar ST, Selvan RK, Ulaganathan M, and Melo JS. Fabrication of Bi_2O_3||AC asymmetric supercapacitor with redox additive aqueous electrolyte and its improved electrochemical performances. *Electrochim. Acta*., 115: 518-524, 2014.

[10] Gujar TP, Shinde VR, Lokhande CD, and Han SH. Electrosynthesis of Bi_2O_3 thin films and their use in electrochemical supercapacitors. *J. Power Sources* 161:1479-1485, 2006.

[11] Zuo W, Zhu W, Zhao D, Sun Y, Li Y, Liu J, and Lou XW. Bismuth oxide: a versatile high-capacity electrode material for rechargeable aqueous metal-ion batteries. *Energy Environ. Sci.* 9: 2881-2891, 2016.

[12] Rudolph, W. W., Mason, R., and Pye, C. C. Aluminium (III) hydration in aqueous solution. A raman spectroscopic investigation and an ab initio molecular orbital study of aluminium (III) water clusters. *Phys. Chem. Chem. Phys*. 2: 5030-5040, 2000.

[13] Lu J, Yang JX, Wang J, Lim A, Wang S, and Loh KP. One-Pot synthesis of fluorescent carbon nanoribbons, nanoparticles, and graphene by the exfoliation of graphite in ionic liquids. *ACS Nano.*, 3: 2367-2375, 2009.

[14] Parvez K, Li R, Puniredd SR, Hernandez Y, Hinkel F, Wang S, Feng X, and Mullen K. Electrochemically exfoliated graphene as solution-processable, highly conductive electrodes for organic electronics. *ACS Nano.,* 7: 3598-3606, 2013.

[15] Parvez K, Wu ZS, Li R, Liu X, Gaf R, Feng X, and Mullen K. Exfoliation of graphite into graphene in aqueous solutions of inorganic salts. *J. Am. Chem. Soc.* 136: 6083-6091, 2014.

[16] Zhang W, Zhu J, Ang H, Zeng Y, Xiao N, Gao Y, Liu W, Hng H. H, and Yan Q. Binder-free graphene foams for O_2 electrodes of Li–O_2 batteries. *Nano.,* 5:9651-9658, 2013.

[17] Yang C, Chen J, Ji X, Pollard, TP, Lu X, Sun CJ, Hou S, Liu Q, Liu C, Qing T, Wang Y, Wang Y, Borodin O, Ren Y, Xu K, and Wang C. Aqueous li-ion battery enabled by halogen conversion-intercalation chemistry in graphite. *Nat.* 569: 245-250, 2019.

[18] Furdin G, Lelaurain M, McRae E, and Marcehe JF, Herold A. Insertion du chloredans le graphite. *Carbo.*, 17: 329-333, 1979.

[19] Das SK, Palaniselvam T, and Adelhelm P. Electrochemical study on the rechargeability of TiO_2 as electrode material for Al-ion batteries with chloroaluminate ionic liquid electrolyte. *Sol. State Ioni.* 340: 115017, 2019.

[20] Zhao Q, Zachman MJ, Sadat WI Al, Zheng J, Kourkoutis LF, and Archer L. Solid electrolyte interphases for high-energy aqueous aluminum electrochemical cells. *Sci. Adv.* 4: 8131, 2018.

[21] Wang, J., Polleux, J., Lim, J., and Dunn, B. Pseudocapacitive contributions to electrochemical energy storage in TiO_2 (anatase) nanoparticles. *J. Phys. Chem. C*, 111:14925-14931, 2007.

[22] Silva AP, Spinelli JE, Noel MM, and Garcia A. Microstructural development during transient directional solidification of hypermonotectic Al–Bi alloys. *Mater. and Design,* 31: 4584-4591, 2010.

[23] Balaya P, Bhattacharyya AJ, Jamnik J, Zhukovskii Yu.F, Kotomin EA, and Maier J. Nano-ionics in the context of lithium batteries. *J. Power Sources,* 159: 171-178, 2006.

[24] Maier J. Nanoionics: ion transport and electrochemical storage in confined systems. *Nat. Mater.,* 4: 805-815, 2005.

[25] Jamnik J, and Maier J. Nanocrystallinity effects in lithium battery materials Aspects of nano-ionics. Part IV. *Phys. Chem. Chem. Phys.* 5: 5215-5220, 2003.

Chapter 3 (Part II)

Bismuth oxychloride (BiOCl): another promising electrode material for Al^{3+} ion storage

Nandi, S., and Das, S. K. *Bull. Mater. Sci*, 44: 1-9, 2021

Bismuth oxychloride (BiOCl): Another promising electrode material for Al^{3+} ion storage

3.2.1 Introduction

In this chapter, the electrochemical activity of Al^{3+} ion storage in bismuth oxychloride (BiOCl) is discussed. Bismuth oxychloride (BiOCl), a layered material has been investigated for varieties of photocatalytic and energy storage applications in recent times [1]. It can be visualized as a sandwich structure where interlacing $[Bi_2O_2]$ layers are placed between two chloride layers [1]. There exists weak van der Waals interaction between the consecutive interlayers, which can facilitate easy transport of charged species in two dimensions. For example, Ye et al. investigated the suitability of BiOCl nanosheets as anode in non-aqueous lithium-ion battery and it was found that it can show discharge capacity of 254 $mAhg^{-1}$ over 15 cycles at a current rate of 500 mAg^{-1} [2]. Similarly, Zhang et al. demonstrated the Na^+ ion storage capability of ultra-thin BiOCl nanoplates in non-aqueous electrolyte with an initial discharge capacity of 1050 $mAhg^{-1}$ at a current rate of 10 mAg^{-1} [3]. Li et al. also reported the K^+ ion storage by BiOCl, where it was shown that discharge capacity of ~ 200 $mAhg^{-1}$ could be achieved over 50 cycles at current density of 50 mAg^{-1} in non-aqueous electrolyte [4]. However, the poor cycling stability of BiOCl, as was observed in all these studies, due to pulverization is a matter of concern. Therefore, in order to address this particular issue, this chapter discusses in detailed the electrochemistry of Al^{3+} ion storage in BiOCl in aqueous electrolyte. It was shown that an optimization of the graphite current collector is necessary for an improved electrochemical performance of BiOCl. A binder-free BiOCl electrode on thermally exfoliated graphite current collector could significantly stabilize the cycling performance. The facile method of processing the exfoliated graphite was adopted from the previous chapter. In addition, the electrochemical performance of BiOCl in various aqueous electrolytes was also investigated and it was found that $AlCl_3$ based aqueous electrolyte is more suitable for enhanced capacity and long-term electrochemical stability. When coupled with an Al anode, BiOCl delivers a stable specific capacity of 145 $mAhg^{-1}$ over 200 cycles.

3.2.2 Experimental Section

3.2.2.1 Materials

Bismuth (III) nitrate pentahydrate [$Bi(NO_3)_3.5H_2O$, Merck], Bismuth (III) iodide [BiI_3, Sigma Aldrich], Ammonium chloride (NH_4Cl, Sigma Aldrich), Acetone, Ethylene glycol [$C_2H_6O_2$, Merck], and Ethanol/Distilled water.

3.2.2.2 Synthesis

One of the objectives of this chapter is to improve the electrochemical stability of BiOCl. For fulfilling this purpose, optimization of the graphite current collector has been performed. Three different types of graphite films were used as current collector in this study. These are labelled as pristine graphite film, exfoliated graphite film and thermally exfoliated graphite film. Pristine graphite film of thickness 0.5 mm was used to obtain the exfoliated and thermally exfoliated graphite films. The exfoliation process of the pristine graphite film was adopted from previous chapter. Briefly, to mention, a dc potential of 3 V was applied for 5 min between two pieces of pristine graphite film in 1 M $AlCl_3$ aqueous electrolyte, which resulted in the exfoliation of the pristine graphite film. This exfoliated graphite film was further heat treated at 800 ^oC for less than a 1 min in air in order to obtain the thermally exfoliated graphite film.

Synthesis of BiOCl: Pristine BiOCl was synthesized by a facile one step hydrothermal method as reported in ref. [5]. In a typical synthesis, 0.97 g of $Bi(NO_3)_3.5H_2O$ and 0.268 g of NH_4Cl was dissolved in 50 ml of ethylene glycol. The mixture was poured in a Teflon autoclave and heated at 180 ^oC for 20 h. The white product was recovered by centrifugation after washing with water/ethanol and dried at 100 ^oC for 12 h.

Synthesis of binder free BiOCl: For the preparation of binder free BiOCl electrode, few pieces of thermally exfoliated graphite films were immersed in the above mixture and performed the heat treatment as described above. The binder free electrodes were collected after the heat treatment and flushed with water/ethanol and dried at 100 ^oC for 12 h. It is noted here that the preparation of thermally exfoliated graphite foil was adopted from the previous chapter.

3.2.2.3 Characterization

The crystallographic phase identification was performed by using powder X-ray diffraction (BRUKER AXS D8 FOCUS; Cu-K_α radiation, λ = 1.5406 Å). The

morphology was observed by scanning electron microscopy (SEM, JEOL JSM 6390LV and ZEISS, SIGMA). X-ray photoelectron spectroscopy (XPS) was recorded by Physical Electronics (PHI 5000 Versa Probe III).

3.2.2.4 Electrochemical analysis

Electrode slurry was made from BiOCl, polyvinylidene fluoride (PVDF) and N-methyl-2-pyrrolidone. The weight ratio of BiOCl and polyvinylidene fluoride is 80:20. This slurry was cast on pristine graphite, exfoliated graphite and thermally exfoliated graphite foils and all of them were dried at 110 ºC for 12 h. Hence, three different types of electrodes were obtained. These were BiOCl coated on pristine graphite, exfoliated graphite and thermally exfoliated graphite current collectors, which are respectively called as BiOCl/G, BiOCl/EG and BiOCl/TEG in this work. The binder free BiOCl electrode is abbreviated as BiOCl/TEG (binder free).

Cyclic voltammetry (CV) and galvanostatic discharge/charge experiments were performed in a conventional three-electrode electrochemical glass cell. Pt electrode and aqueous Ag/AgCl electrode were used as the counter and reference electrodes respectively while BiOCl/G, BiOCl/EG and BiOCl/TEG acts as the working electrode. The discharge/charge and CV experiments were performed in the voltage range of -0.8 V to 0.3 V and -1 V to 0.3 V respectively. Electrochemical impedance spectra were obtained by scanning in the frequency range of 1 mHz-200 kHz at signal amplitude of 10 mV.

An aqueous Al-ion full cell was tested with Al metal as anode and BiOCl as cathode. Typically used Al foil (Hindalco Freshwrapp) for household purposes was utilized for this purpose. The utilized electrolyte was 1 M $AlCl_3.6H_2O$ aqueous solution. The galvanostatic discharge/charge and CV experiments were performed in the voltage range of 0-1.2 V considering BiOCl/G, BiOCl/EG and BiOCl/TEG as the working electrode and Al as both the reference and counter electrodes. For ex-situ XRD, SEM and XPS experiments, the electrodes were harvested after required number of discharge/charge cycles and dried at 110 ºC for 24 h. All the electrochemical experiments were conducted at room temperature (25 ºC) and ambient atmosphere.

Bismuth oxyiodide (BiOI) was prepared by direct thermal treatment of bismuth (III) iodide (BiI_3) as reported by Chen et al [6]. Briefly, 1 g of BiI_3 was put in a crucible container and heated at 300 ^oC for 8 h. The red product was collected by washing with ethanol and distilled water for a few times, and dried at 60 ^oC for 12 h.

3.2.3 Results and Discussion

Figure 3.2.1 (a-c) shows the SEM images of pristine graphite, exfoliated graphite and thermally exfoliated graphite films. It is evident that the surface of the electrochemically exfoliated graphite and thermally exfoliated graphite are covered with nanoflakes (Figure 3.2.1b, c). The digital photographs of these graphite films are also shown in Figure 3.2.1 (d-f). It is observed that the thicknesses of the exfoliated graphite and the thermally exfoliated graphite are quite larger than the pristine graphite film (0.5 mm). The respective thickness values are 0.78 mm and 2.02 mm. It signifies that thermally exfoliated graphite is more porous in nature which is quite beneficial to enhance the electrode and electrolyte contact area.

The XRD patterns (Figure 3.2.2) indicate the graphitic structure of all these graphite films. In addition, XRD pattern of BiOCl (Figure 3.2.3a) shows that the synthesized material is crystallized in tetragonal crystal phase of BiOCl (JCPDS 06-0249), space group *P*4/*nmm*. The binder free BiOCl electrode also possesses the similar crystal structure. FESEM investigation (Figure 3.2.3b, c) shows spherical clusters of BiOCl which is composed of nanoflakes.

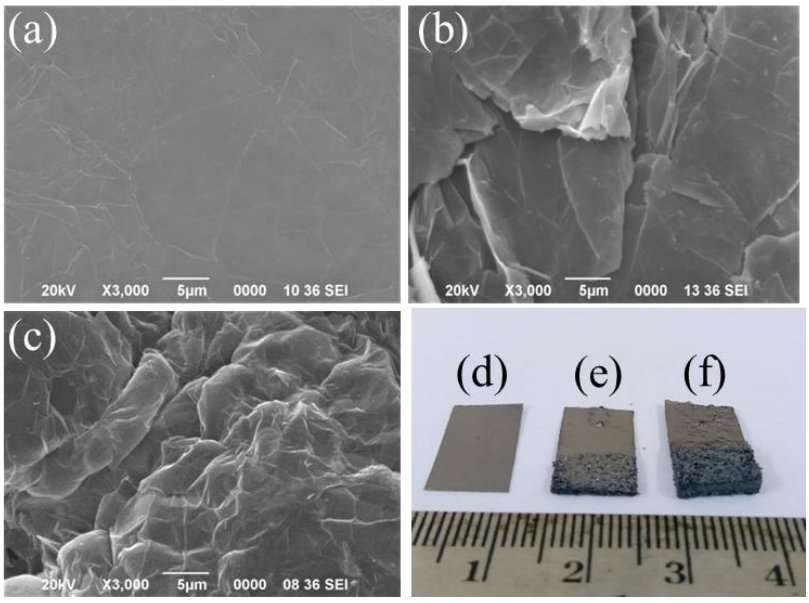

Figure 3.2.1 SEM and digital images of (a, d) pristine graphite, (b, e) exfoliated graphite, (c, f) thermally exfoliated graphite films.

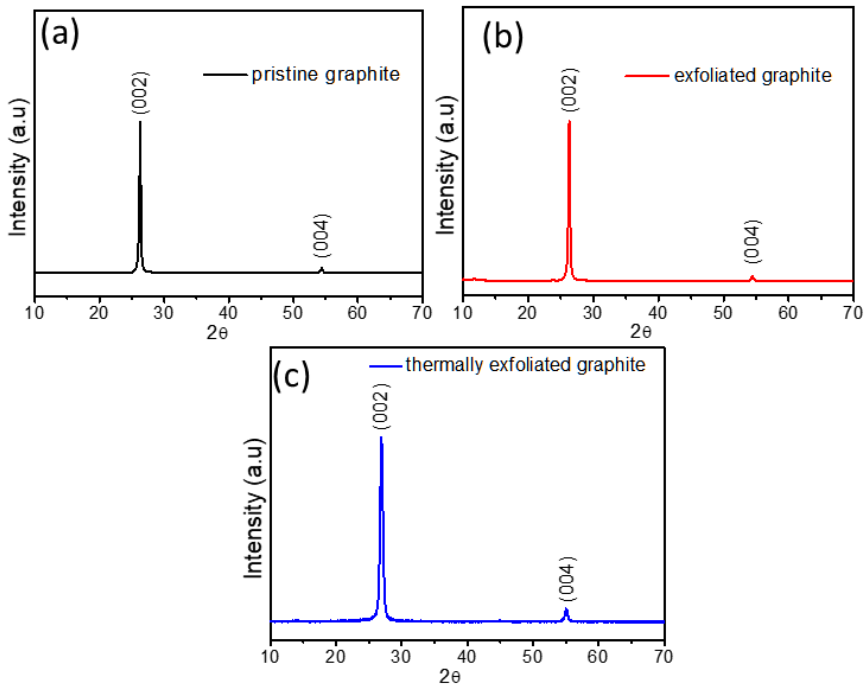

Figure 3.2.2 XRD patterns of (a) pristine graphite, (b) exfoliated graphite, and (c) thermally exfoliated graphite films.

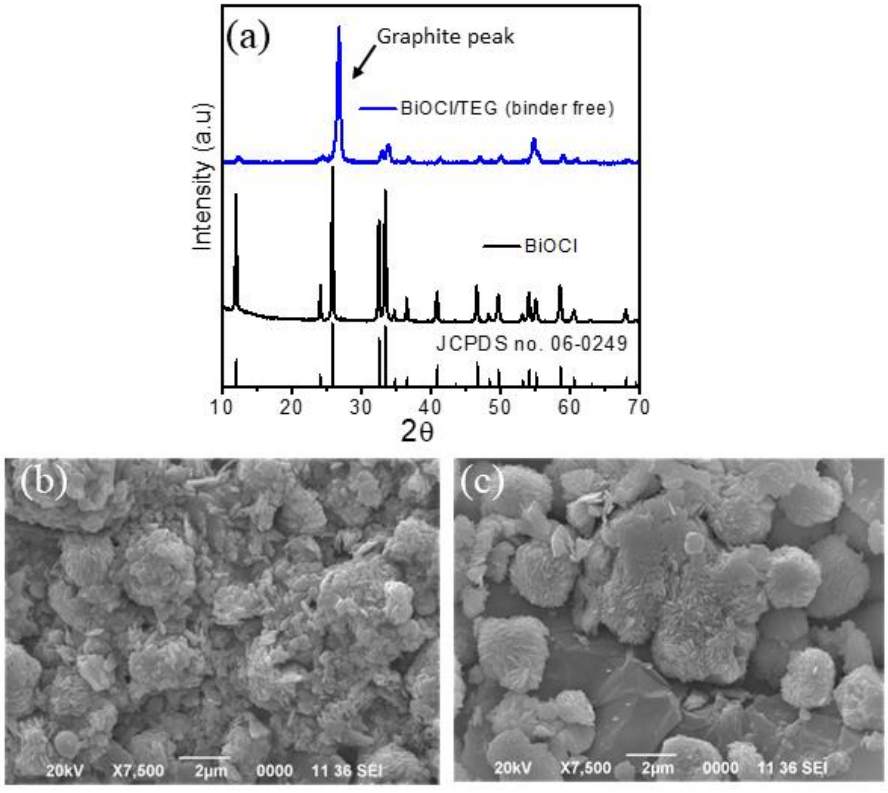

Figure 3.2.3 (a) XRD pattern of BiOCl and BiOCl/TEG (binder free) electrode, (b-c) SEM images of BiOCl/G and BiOCl/TEG (binder free).

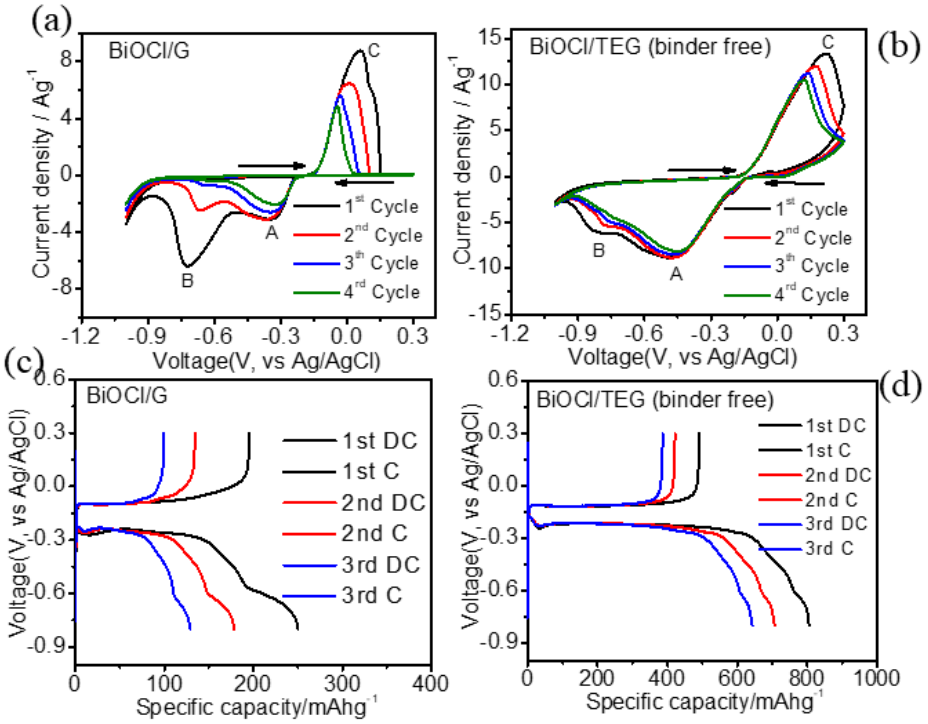

Figure 3.2.4 CV profiles of (a) BiOCl/G and (b) BiOCl/TEG (binder free) at a scan rate of 2.5 mVs^{-1}. Galvanostatic discharge/charge profiles of (c) BiOCl/G and (d) BiOCl/TEG (binder free) at a specific current rate of 2.5 A g^{-1} in 1 M $AlCl_3$ aqueous electrolyte.

In order to identify the Al^{3+} ion electrochemical activity in BiOCl, cyclic voltammetry and galvanostatic discharge/charge experiments were initially performed on BiOCl/G and binder free BiOCl (i.e. BiOCl/TEG (binder free)) electrodes in 1 M $AlCl_3$ aqueous electrolyte in a conventional three electrode electrochemical cell. Figure 3.2.4a shows the CV profile of BiOCl/G at a scan rate of 2.5 mVs^{-1}. It shows two prominent cathodic redox peaks, designated as A and B in the Figure, at -0.35V and -0.72 V respectively and one anodic peak at 0.05 V (peak C) in the first cycle. The current response for peak B severely decreases with increasing cycle number. A decrease in current response for peak A and C is also noticed. Similarly, as shown in Figure 3.2.4b, redox peaks A and C could also be profoundly noticed in case of BiOCl/TEG (binder free). However, peak B could be marginally observed and the current response is not severely decreasing unlike BiOCl/G electrode. Galvanostatic discharge/charge experiments also corroborate the cyclic voltammetry results. Figure 3.2.4c and Figure 3.2.4d shows the discharge/charge profiles of BiOCl/G and BiOCl/TEG (binder free) respectively in 1 M $AlCl_3$ aqueous electrolyte in the voltage

range of -0.8 V to 0.3 V (vs. Ag/AgCl) at a current rate of 2.5 Ag^{-1}. In both cases, flat charge/discharge profiles could be observed. The discharge and charge plateaus are located at -0.22 V and -0.11 V respectively. However, noticeable difference in the storage capacities could be observed. As could be seen from the variation of capacity with cycle number (Figure 3.2.5), the binder free electrode outperforms the BiOCl/G electrode. The first cycle discharge and charge capacities are 805 $mAhg^{-1}$ and 490 $mAhg^{-1}$ respectively for the BiOCl/TEG (binder free) electrode, whereas these values are only 250 $mAhg^{-1}$ and 195 $mAhg^{-1}$ for BiOCl/G. The 80^{th} cycle discharge capacities for BiOCl/TEG (binder free) and BiOCl/G are 316 $mAhg^{-1}$and 3.5 $mAhg^{-1}$ respectively. Another important feature is that almost 77 % of discharge capacity is seen in the plateau region in the first discharge cycle for BiOCl/TEG (binder free), whereas only 57 % could be seen for BiOCl/G. It is to be noted that a flat discharge plateau is very much important for maintaining a stable energy density for batteries. A comparison of the CV profiles (Figure 3.2.6) indicates that neither the pristine graphite film nor the thermally exfoliated graphite film exhibits any electrochemical activity in the measured potential range. CV experiments were also performed with 0.5 M $Al_2(SO_4)_3$ and 1 M $Al(NO_3)_3$ aqueous electrolytes with BiOCl/TEG (binder free) electrode. The CV profiles (Figure 3.2.7a) are almost identical for $AlCl_3$ and $Al_2(SO_4)_3$ aqueous electrolytes. However, the CV profile (Figure 3.2.7b) obtained in $Al(NO_3)_3$ aqueous electrolyte shows sharp decrease in current in the negative potential with difficulty to observe the cathodic peak. Similar trend was also noticed for previously reported other electrode materials [7-10]. Again, galvanostatic discharge/charge experiment (Figure 3.2.8) performed with BiOCl/TEG (binder free) in $Al_2(SO_4)_3$ aqueous electrolyte at a current rate of 2.5 Ag^{-1} shows very low specific capacities in comparison to $AlCl_3$ aqueous electrolyte.

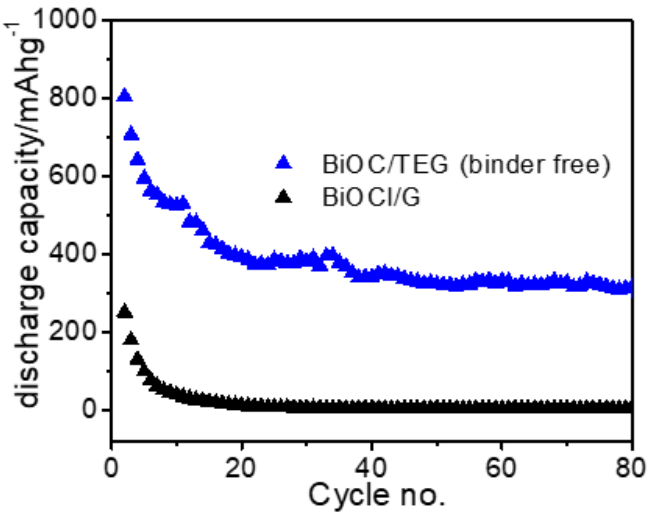

Figure 3.2.5 Variation of discharge capacities with cycle number at a current rate of 2.5 A g^{-1} in 1 M $AlCl_3$ aqueous electrolyte.

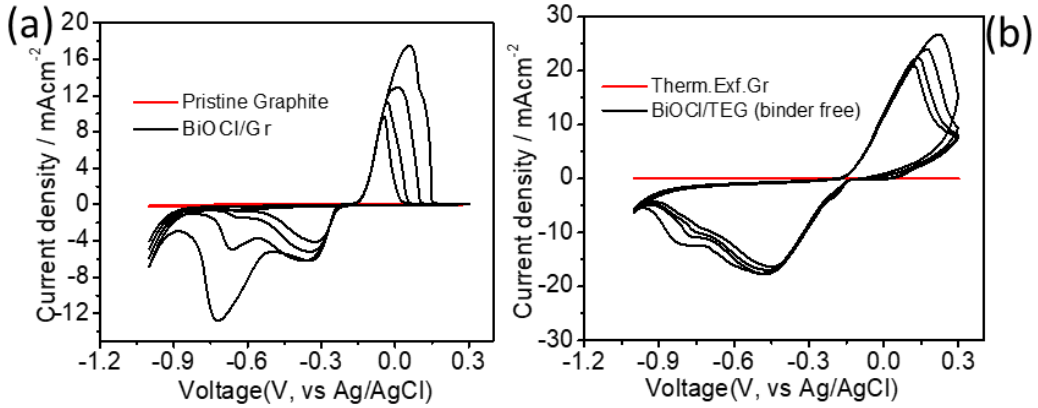

Figure 3.2.6 CV profiles of (a) pristine graphite, and (b) thermally exfoliated graphite at a scan rate of 2.5 mVs^{-1} in 1 M $AlCl_3$ aqueous electrolyte.

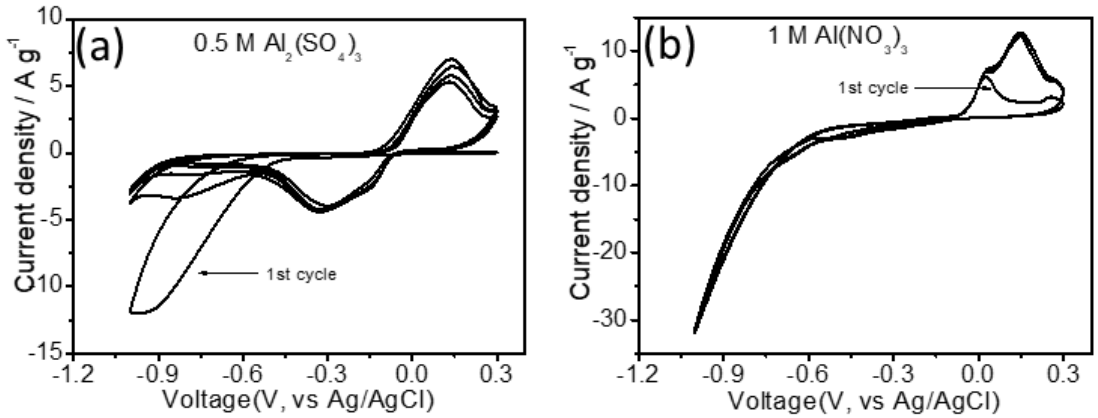

Figure 3.2.7 (a) CV profiles of BiOCl/TEG (binder free) in (a) 0.5 M $Al_2(SO_4)_3$, and (b) 1 M $Al(NO_3)_3$ at a scan rate of 2.5 mVs^{-1}.

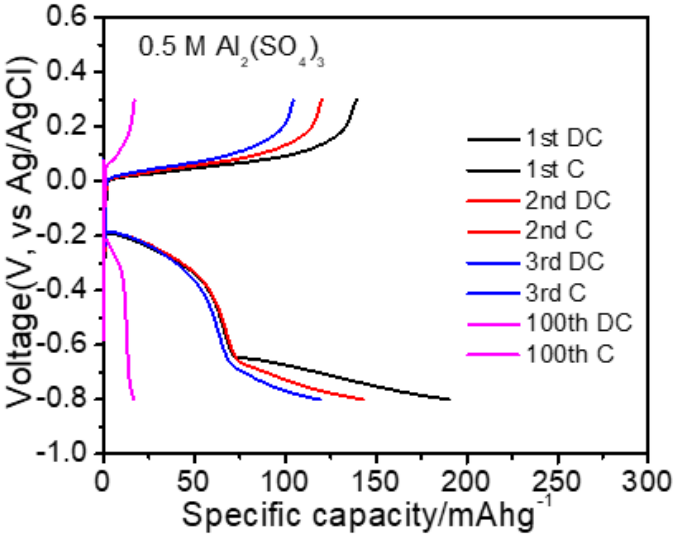

Figure 3.2.8 Galvanostatic discharge/charge profile of BiOCl/TEG (binder free) in 0.5 M $Al_2(SO_4)_3$ aqueous electrolyte at a current rate of 2.5 A g^{-1}.

To verify the effect of other cations, CV experiments were performed with 1 M LiCl, 1 M NaCl and 1 M $MgCl_2$ aqueous electrolytes at scan rate of 2.5 mVs^{-1}. The CV profiles (Figure 3.2.9) obtained in LiCl and NaCl aqueous electrolytes are almost similar. One pair of prominent cathodic and anodic redox peaks could be observed at -0.83 V and 0.06V respectively. On the other hand, two major anodic peaks at -0.29 V and -0.1 V and one cathodic peak at -0.9 V could be seen in case of $MgCl_2$ aqueous electrolyte (Figure 3.2.9c). However, a comparison of the CV profiles indicate that the potential positions of the cathodic peaks observed with LiCl, NaCl and $MgCl_2$ electrolytes do not match with the potential observed for $AlCl_3$ electrolyte (Figure 3.2.10). It thus suggests the electroactivity of Al^{3+} ion in BiOCl.

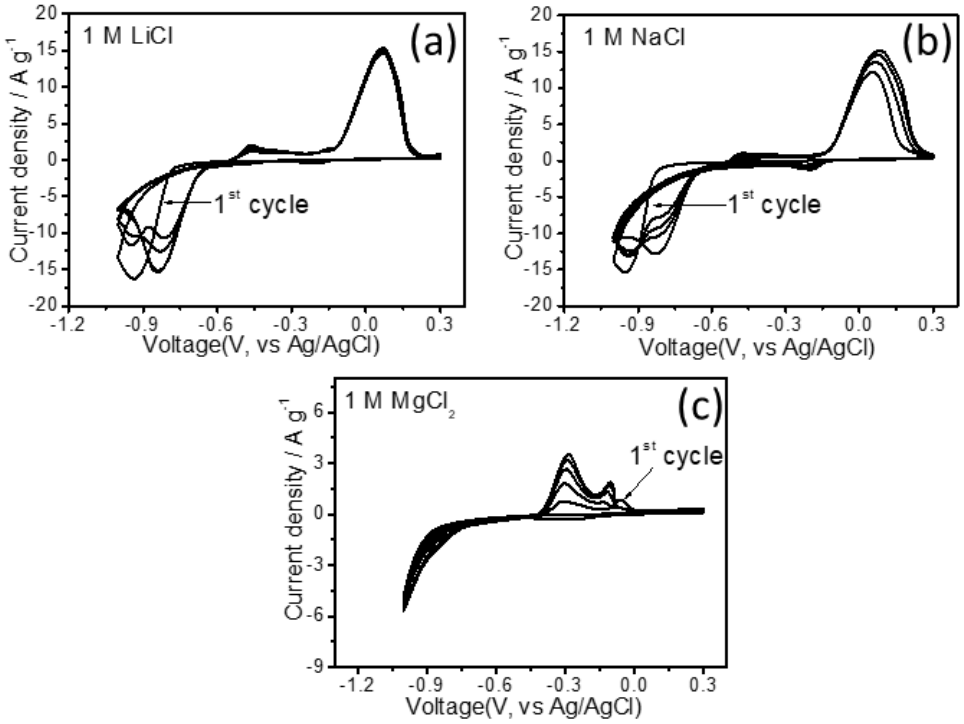

Figure 3.2.9 CV profiles of BiOCl/TEG (binder free) in (a) 1 M LiCl, (b) 1 M NaCl, and (c) 1 M $MgCl_2$ aqueous electrolytes at a scan rate of 2.5 mVs^{-1}

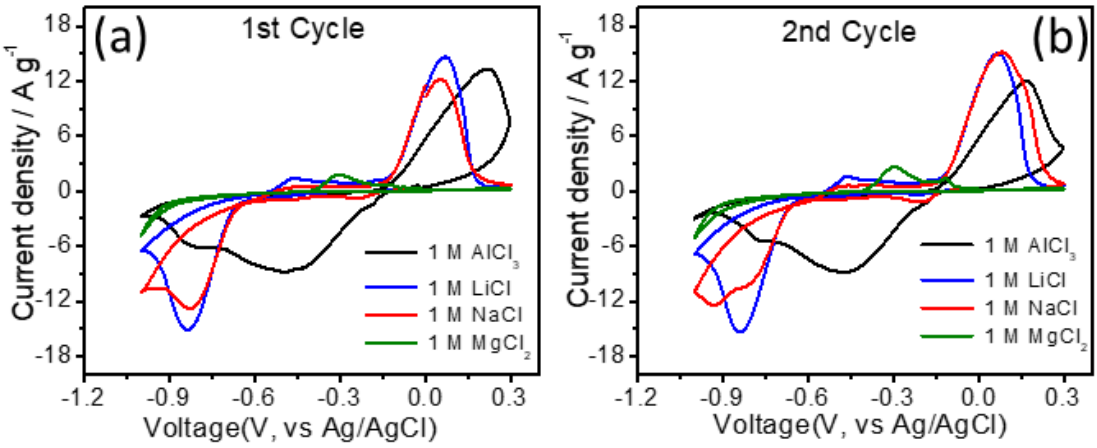

Figure 3.2.10 Comparison of CV profiles of BiOCl/TEG (binder free) obtained in 1 M $AlCl_3$, 1 M LiCl, 1 M NaCl, 1 M $MgCl_2$ aqueous electrolytes at a scan rate of 2.5 mVs^{-1}, (a) 1st cycle, and (b) 2nd cycle.

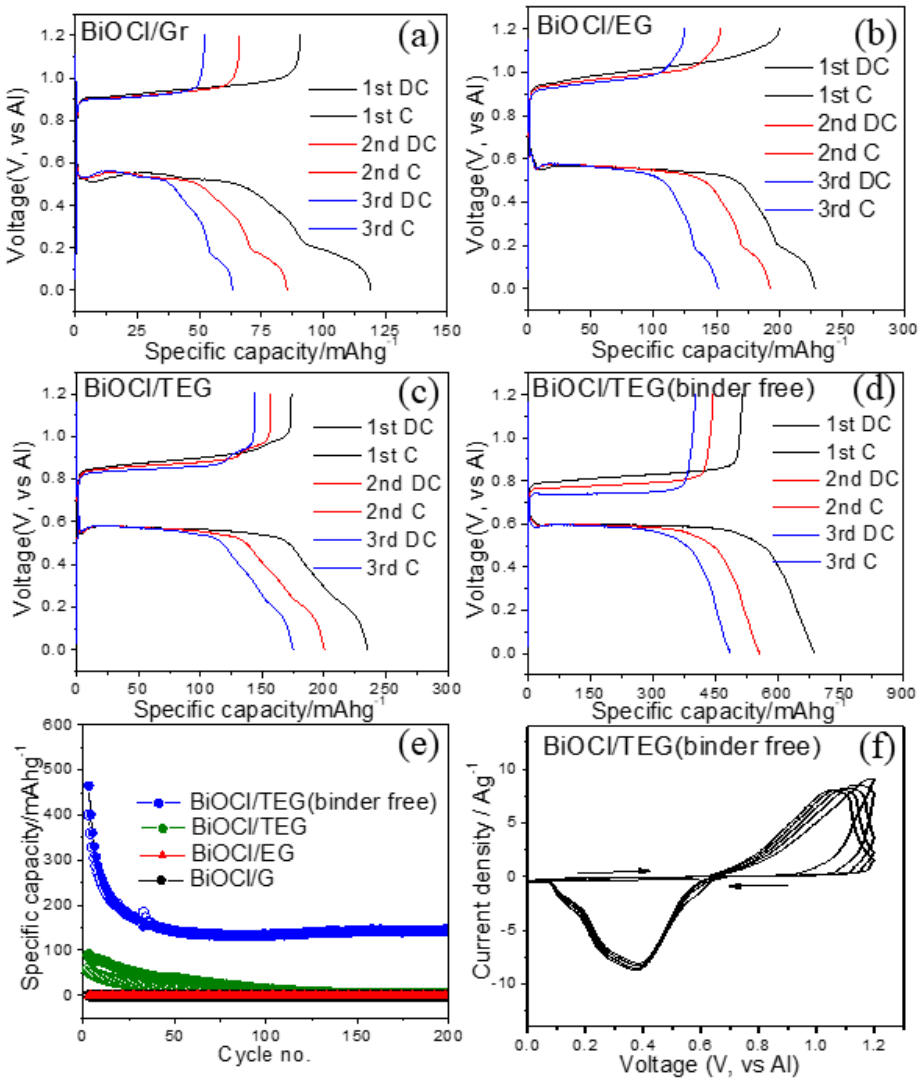

Figure 3.2.11 Galvanostatic discharge/charge profiles of (a) BiOCl/G, (b) BiOCl/EG, (c) BiOCl/TEG, (d) BiOCl/TEG (binder free) at a specific current rate of 1 A g^{-1}. (e) Variation of discharge capacities with cycle number at a current rate of 2.5 A g^{-1}. (f) CV profile of Al- BiOCl/TEG (binder free) at a scan rate of 2.5 mVs^{-1} in 1 M $AlCl_3$ aqueous electrolyte. The potential is measured with respect to Al electrode.

Armed with this knowledge of Al^{3+} ion electrochemistry of BiOCl, further electrochemical investigation of BiOCl was made in a full-cell configuration by pairing Al metal as anode in 1 M $AlCl_3$ aqueous electrolyte. The previous chapter suggest that aqueous electrolyte of $AlCl_3$ is beneficial for better functioning of Al-metal batteries. It is because $AlCl_3$ aqueous electrolyte can effectively remove the inherently present passivating oxide layer from the Al metal surface, which is otherwise difficult in case of $Al_2(SO_4)_3$ and 1 M $Al(NO_3)_3$ aqueous electrolytes. Four

full-cells were assembled with BiOCl/G, BiOCl/EG, BiOCl/TEG and BiOCl/TEG (binder free) electrodes. Figure 3.2.11(a-d) shows the respective galvanostatic discharge/charge profiles at a current rate of 1 Ag^{-1}. It could be observed that all the cells exhibit good reversibility with varying degree of specific capacities. The highest specific capacities are shown by BiOCl/TEG (binder free) with first cycle discharge and charge capacity values of 687 $mAhg^{-1}$ and 514 $mAhg^{-1}$ respectively (Figure 3.2.11d). On the other hand, these values are only 119 $mAhg^{-1}$ and 90 $mAhg^{-1}$ for BiOCl/G (Figure 3.2.11a), 229 $mAhg^{-1}$ and 200 $mAhg^{-1}$ for BiOCl/EG (Figure 3.2.11b), 235 $mAhg^{-1}$ and 172 $mAhg^{-1}$ for BiOCl/TEG (Figure 3.2.11c). The electrochemical cycling stability was investigated at a high current rate of 2.5 Ag^{-1}. As shown in Figure 3.2.11e, Al-BiOCl/TEG (binder free) cell showed the best performance. Although there is an initial decline of specific capacities, these values got stabilized after 50^{th} cycle with discharge capacity value of 145 $mAhg^{-1}$ at the 200^{th} cycle. Contrarily, rest of the Al-cells could not sustain the current rate of 2.5 Ag^{-1}. Al-BiOCl/TEG cell could show specific capacities but these values are quite inferior in comparison to Al-BiOCl/TEG (binder free). The discharge capacity values are only 36 $mAhg^{-1}$ and 12 $mAhg^{-1}$ at the 50^{th} and 100^{th} cycle respectively. The high degree of reversibility is also reflected from the CV profiles (Figure 3.2.11f). A pair of highly reversibly redox peaks could be seen at 0.4 V and 1 V. It is noted here that the contribution of the graphite/exfoliated graphite/thermally exfoliated graphite current collector in estimating the specific capacities of BiOCl is very negligible. It should not be confused with the previous work since the voltage range and current rate are completely different in this present chapter. The inactivity of these current collectors is well evidenced from the charge-discharge experiments performed with the bare current collectors (i.e. without any BiOCl) at the same current rate (Figure 3.2.12). The inactivity was also evidenced from the CV profiles as discussed earlier (Figure 3.2.6). Another interesting feature of the charge-discharge profiles of the Al-BiOCl cells is the existence of flat discharge and charge plateaus in all cells. The discharge and charge potential plateaus are respectively observed at 0.6 V and 0.8 V (vs Al) for Al-BiOCl/TEG (binder free) cell. The polarization (estimated as the difference between the discharge and charge potentials at half of the capacity values) is found to be lowest (= 0.17 V) for Al-BiOCl/TEG (binder free) cell. These values are in the range of 0.3-0.4 V for rest of the Al-BiOCl cells. An estimation of charge transfer resistance by electrochemical impedance spectroscopy (EIS) shows the lowest

resistance for Al-BiOCl/TEG (binder free) cell. The EIS spectra are shown in Figure 3.2.13a. The decreasing order of the charge transfer resistance is as follows: BiOCl/G > BiOCl/EG > BiOCl/TEG > BiOCl/TEG (binder free). This is very much consistent with the overall electrochemical stability data. It is expected that the direct growth of BiOCl on the thermally exfoliated graphite could provide better electrical contact and easy pathways for Al^{3+} ion transport.

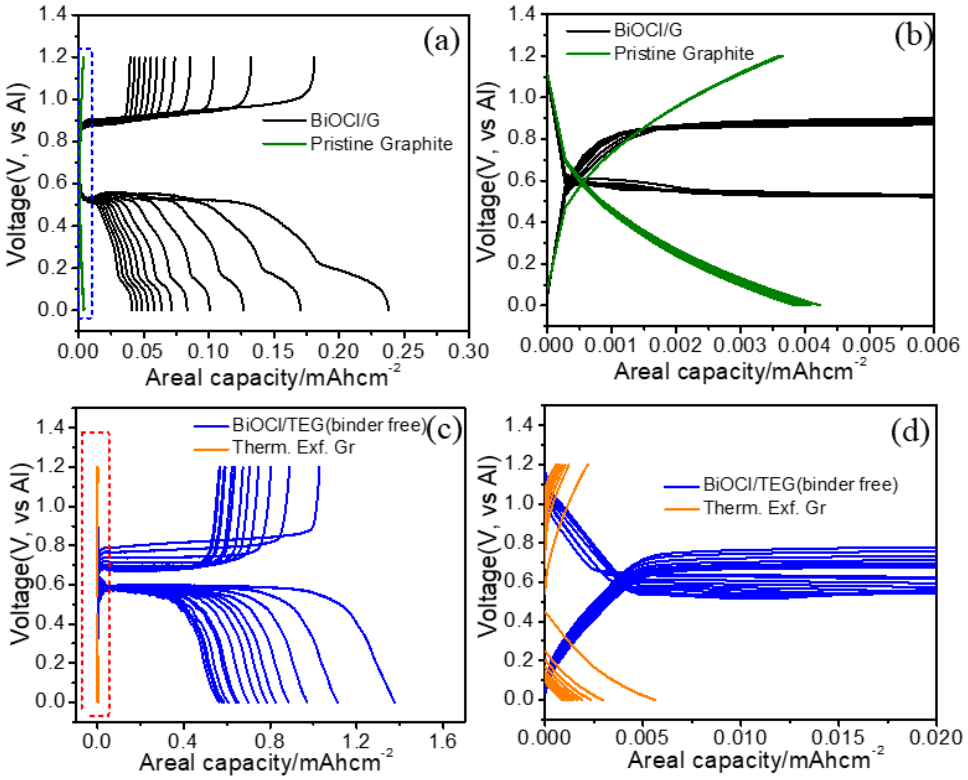

Figure 3.2.12 Comparison of galvanostatic discharge/charge profiles of (a) pristine graphite/ BiOCl/G, and (c) thermally exfoliated graphite/ BiOCl/TEG (binder free) at a current rate of 2 $mAcm^{-2}$. (b-d) Enlarged view of dotted blue and red box to show the discharge/charge profiles of pristine graphite and thermally exfoliated graphite.

Structural evolution of the BiOCl electrodes before and after discharge was investigated by ex-situ XRD analysis. Figure 3.2.13b (and Figure 3.2.14) shows the ex-situ XRD patterns of the electrodes. Titanium (Ti) was used as the current collector for performing this measurement so that the intense (002) peak from graphite current collector could be avoided. It is noted here that the BiOCl peaks are not so clearly visible due to high intensity (002) diffraction peak from the graphite substrate (Figure 3.2.3a). The analysis of the patterns was difficult due to the superimposition of large number of diffraction peaks of BiOCl, Bi_2O_3, Bi, Al_2O_3 and Ti. However, few of the

peaks 2θ = 13.74°, 16.45°, 18.15°, 41.67° and 57.27° seen after discharge could be identified from the Al_2O_3 phase (JCPDS nos. 16-0394 and 23-1009). The Bi peaks (2θ = 37.98° and 39.68°) are superimposed with Ti phase. Absence of major Bi_2O_3 peaks suggests it could be in amorphous or nanocrystalline phase. Ex-situ SEM images of the discharge state electrode show the morphological change of BiOCl after discharge (Figure 3.2.13c). As shown in Figure 3.2.13c, tiny flakes could be seen in comparison to spherical clusters as was observed for pristine BiOCl. During the charged state, the intensity of the prominent peaks from Al_2O_3 phase diminishes. Ex-situ XPS investigation was carried out to further understand the electrochemical process. As shown in Figure 3.2.13d, the Bi 4*f* peaks could be located at 160.15 eV and 165.43 eV after discharge. Whereas these peaks are located at 158.02 eV and 163.27 eV in case of pristine BiOCl. This shift may be attributed to the interaction of Al^{3+} ions with BiOCl during discharge similar to Li^+, Na^+ and K^+ ions [2-4]. During charge, the Bi 4*f* peaks again shift to lower binding energies although these could not be seen overlapping with the pristine BiOCl spectrum. The XPS survey spectrum of BiOCl/TEG (binder free) is also shown in Figure 3.2.15. There is also a change in the O 1s spectrum (Figure 3.2.13e). The peaks shift to higher binding energies during discharge. The new peaks are at 530.8 eV and 533.3 eV. These binding energies correspond to Al_2O_3, which again signifies the possibility of formation of Al-O bond [11-12]. Similarly, there is a pronounced shift in the Cl 2*p* peaks (Figure 3.2.16). Al 2p peak at 75.6 eV could also be observed for the discharged state BiOCl which also confirms presence of Al [11]. Therefore, based on these observations, it could be commented that there is a conversion type of electrochemical reaction that undergoes while Al^{3+} ion electrochemically react with BiOCl. Similar type of conversion reaction was also observed for Li^+, Na^+ and K^+ ions [2-4]. The following two types of reversible electrochemical reactions are possible during the discharge process: (i) $3BiOCl + Al^{3+} + 3e^- \rightarrow Bi_2O_3 + Bi + AlCl_3$ and (ii) $Bi_2O_3 + 2Al^{3+} + 6e^- \rightarrow 2Bi + Al_2O_3$. It is noted here that the potential plateaus of BiOCl is almost identical to Bi_2O_3 in the previous chapter, which signifies similar kind of storage mechanism. Complete reversible conversion of Al_2O_3 may not be possible as indicated by the existence of Al 2*p* during charging which was observed at slightly lower binding energy (74.6 eV). CV experiments were also performed at different scan rates (Figure 3.2.17) to determine any relationship between the peak current responses (I) for both the cathodic and anodic redox peaks and the scan rates (γ) according to the equation

$I=k\gamma^{0.5}$ (k is a constant). However, it does not follow any linear relationship ruling out the possibility of diffusion-controlled Al^{3+} ion insertion/extraction process [13-14]. In addition to BiOCl, other bismuth oxyhalides may also act as an electrode material for aqueous Al-metal battery. The Al^{3+} ion electroactivity of BiOI is also investigated. The XRD pattern (Figure 3.2.18a) of BiOI matches well with the tetragonal phase of BiOI, space group *P*4/*nmm*, (JCPDS no. 10-0445). As shown in Figure 3.2.18b, the CV profiles clearly exhibits redox peaks for BiOI. The discharge/charge profiles (Figure 3.2.18c) are similar to BiOCl. However, the specific capacity values are lower in comparison to BiOCl

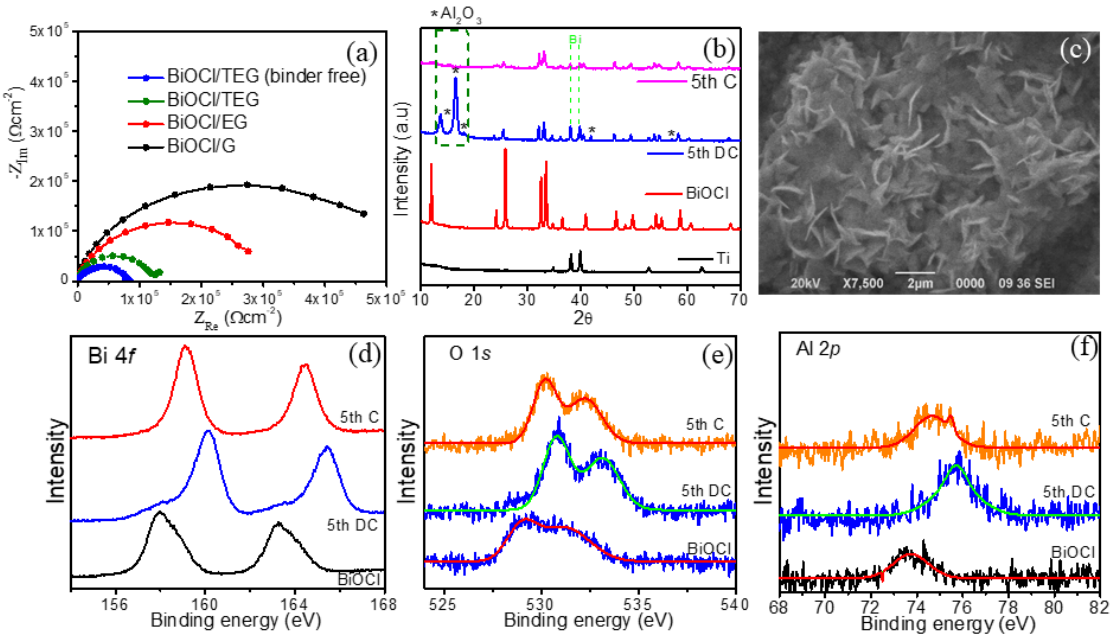

Figure 3.2.13 (a) Electrochemical Impedance Spectroscopy (EIS) for BiOCl/G, BiOCl/EG, BiOCl/TEG and BiOCl/TEG (binder free). (b) ex-situ XRD patterns before discharge, after 5th discharge and after 5th charge, (c) SEM image of BiOCl/TEG (binder free) after discharge, and ex-situ XPS spectra for (d) Bi 4*f*, (e) O 1*s*, (f) Al 2*p* of BiOCl/TEG (binder free) before discharge, after 5th discharge and after 5th charge respectively.

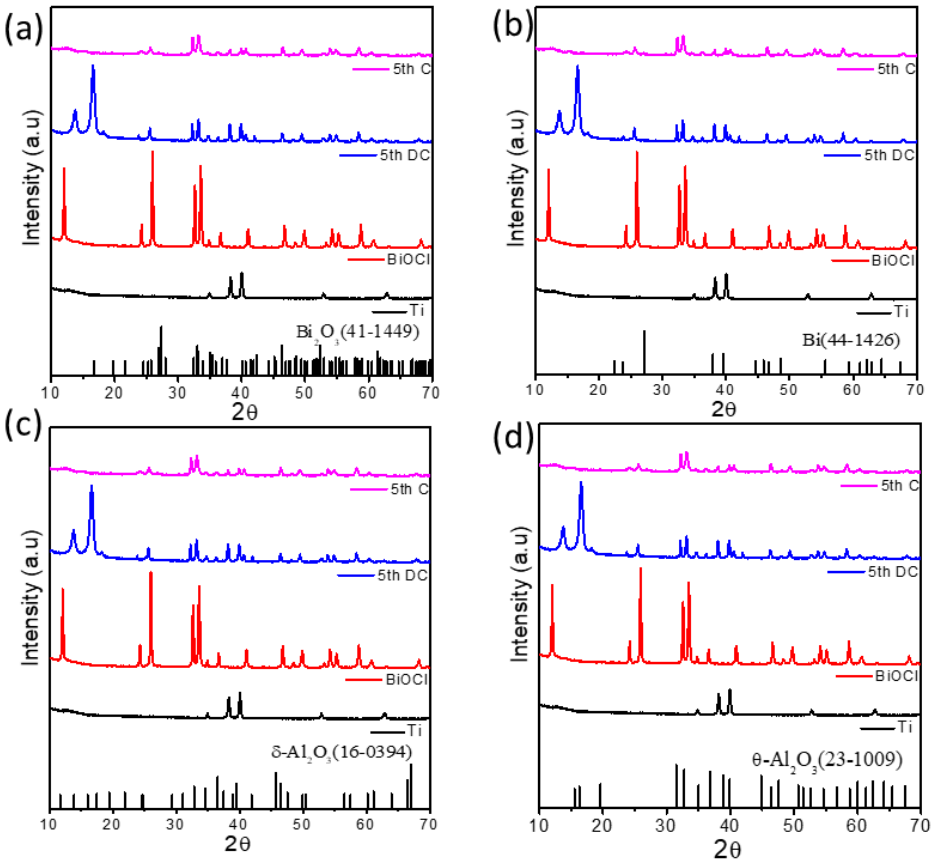

Figure 3.2.14 Ex-situ XRD patterns of BiOCl/TEG (binder free) after 5th discharge and 5th charge. The JCPDS numbers were plotted separately with (a) Bi_2O_3, (b) Bi, (c) δ-Al2O3 and, (d) θ-Al_2O_3 respectively.

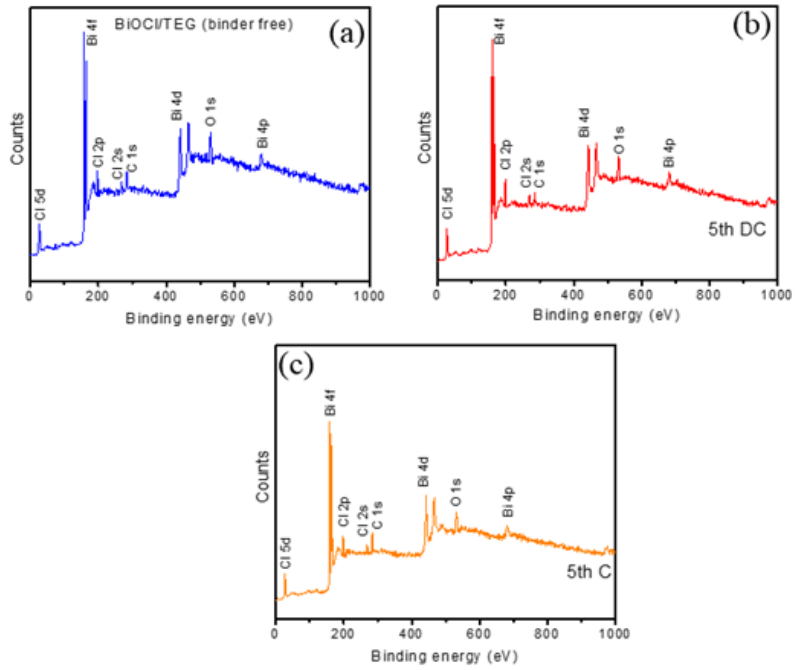

Figure 3.2.15 XPS survey spectrum of BiOCl/TEG (binder free), (a) before discharge, (b) after 5th discharge (5th DC), and (c) after 5th charge (5th C) states.

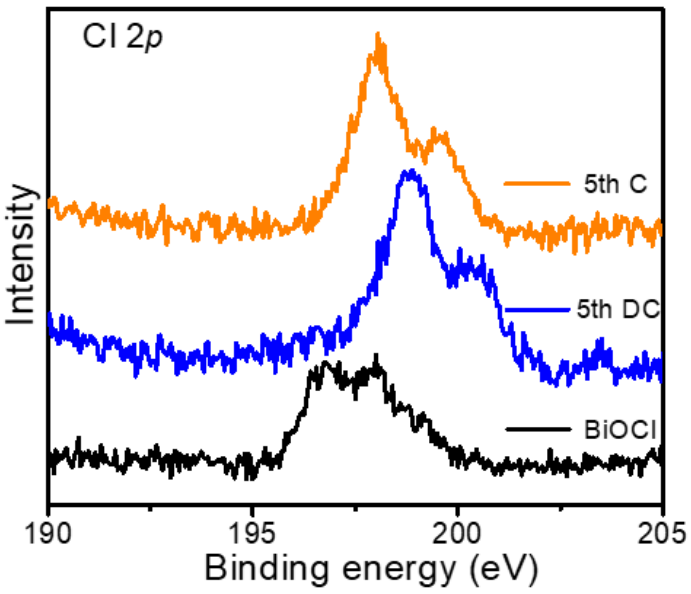

Figure 3.2.16 Cl 2*p* XPS spectra of BiOCl/TEG (binder free) before discharge, after 5^{th} discharge (5^{th} DC) and 5^{th} charge (5^{th} C) states.

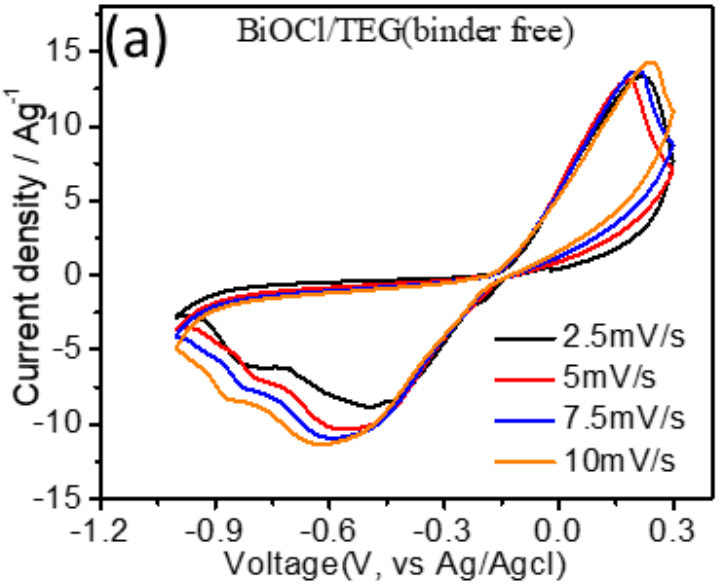

Figure 3.2.17 CV profiles of BiOCl/TEG (binder free) in 1 M $AlCl_3$ aqueous electrolyte at different scan rates.

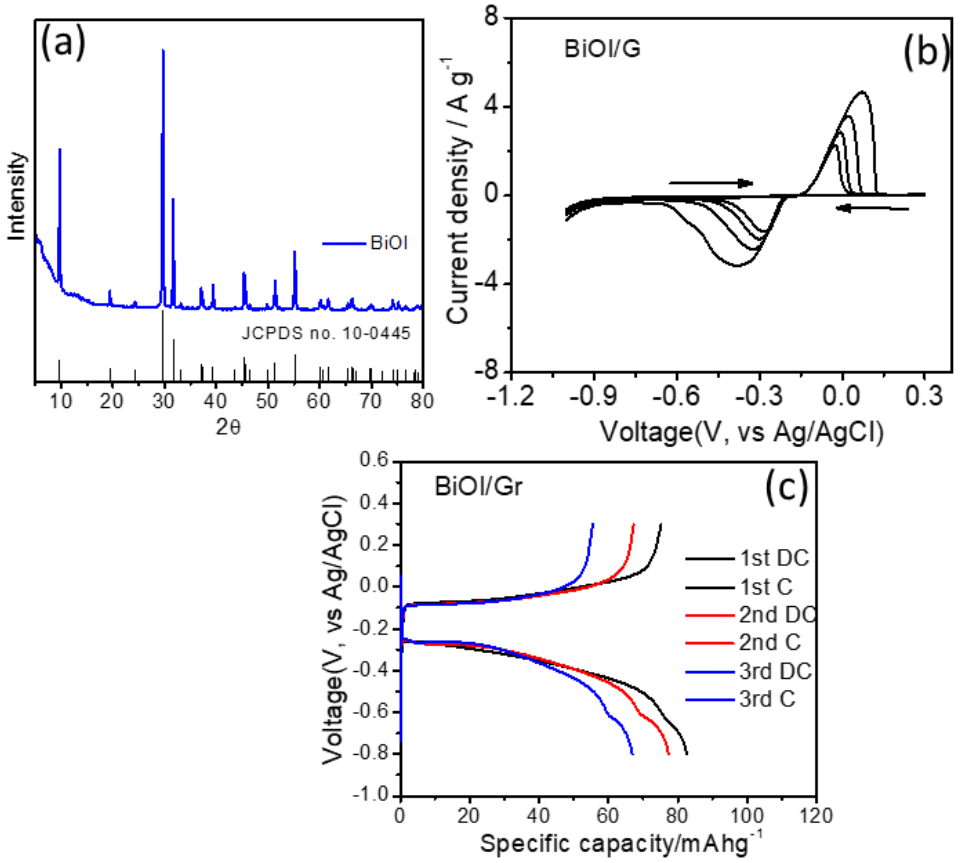

Figure 3.2.18 (a) XRD pattern of BiOI, (b) CV profile of BIOI/G at a scan rate of 2.5 mVs^{-1}, and (c) galvanostatic discharge/charge profile of BIOI/G in 1 M $AlCl_3$ aqueous electrolyte at a specific current rate of 2.5 A g^{-1}.

3.2.4 Conclusion

In summary, the Al^{3+} ion storage behavior of BiOCl in aqueous electrolyte is illustrated. When coupled with an Al anode, BiOCl delivers a stable specific capacity of 145 $mAhg^{-1}$ over several cycles. It was also shown that an optimization of the graphite current collector is necessary for an improved electrochemical performance of BiOCl. A binder free BiOCl electrode on thermally exfoliated graphite current collector could significantly stabilize the cycling performance of the investigated Al-metal cells.

3.2.5 References

[1] Di, J., Xia, J., Li, H., Guo, S., and Dai, S. Bismuth oxyhalide layered materials for energy and environmental applications. *Nano. Energy.*, 41, 172–192, 2017.

[2] Ye, L., Wang, L., Xie, H., Su, Y., Jin, X., and Zhang, C. Two-dimensional layered BiOX (X= Cl, Br) compounds as anode materials for lithium-ion batteries. *Energy Technol.*, 3:1115–1120, 2015.

[3] Zhang, Y., Lu, S., Wang, M.-Q., Niu, Y., Liu, S., Li, Y., Wu, X., Bao, S.-J., and Xu, M. Bismuth oxychloride ultrathin nanoplates as an anode material for sodium-ion batteries. *Mater. Lett.*, 178: 44–47, 2016.

[4] Li, W., Xu, Y., Dong, Y., Wu, Y., Zhang, C., Zhou, M., Fu, Q., Wu, M., and Lei, Y. Bismuth oxychloride nanoflake assemblies as a new anode for potassium ion batteries. *Chem. Commun.*, 55: 6507–6510, 2019.

[5] Zhu, Q., Cheng, M., Yang, X., Zhang, B., Wan, Z., Xiao, Q., and Yu, Y. Self-supported ultrathin bismuth nanosheets acquired by in-situ topotactic transformation of BiOCl as a high-performance aqueous anode material. *J. Mater. Chem. A.*, 7:6784–6792, 2019.

[6] Chen, C., Hu, P., Hu, X., Mei, Y., and Huang, Y. Bismuth oxyiodide nanosheets: a novel high-energy anode material for lithium-ion batteries. *Chem. Commun.*, 51:2798–2801, 2015.

[7] Liu, S., Pan, G. L., Li, G. R., and Gao, X. P. Copper hexacyanoferrate nanoparticles as cathode material for aqueous Al-ion batteries. *J. Mater. Chem. A.*, 3: 959–962, 2015.

[8] Lahan, H., and Das, S. K. Al^{3+} ion intercalation in MoO_3 for aqueous aluminum-ion battery. *J. Power Sources*, 413:134–138, 2019.

[9] Liu, S., Hu, J. J., Yan, N. F., Pan, G. L., Li, G. R., and Gao, X. P. Aluminum storage behavior of anatase TiO_2 nanotube arrays in aqueous solution for aluminum ion batteries. *Energy Environ. Sci.*, 5: 9743–9746, 2012.

[10] Lahan, H., Boruah, R., Hazarika, A., and Das, S. K. Anatase TiO_2 as an anode material for rechargeable aqueous aluminum-ion batteries: remarkable graphene induced aluminum ion storage phenomenon. *J. Phys. Chem. C*, 121: 26241–26249, 2017.

[11] Liu, Q., Qin, H., Boscoboinik, J. A., and Zhou, G. Comparative study of the oxidation of NiAl (100) by molecular oxygen and water vapor using ambient-pressure X-ray Photoelectron Spectroscopy. *Langm.*, 32:11414–11421, 2016.

[12] Chen, C., Splinter, S. J., Do, T., and McIntyre, N. S. Measurement of oxide film growth on Mg and Al surfaces over extended periods using XPS. *Surf. Sci.*, 382: L652–L657, 1997.

[13] Wang, J., Polleux, J., Lim, J., and Dunn, B. Pseudocapacitive contributions to electrochemical energy storage in TiO_2 (anatase) nanoparticles. *J. Phys. Chem. C*, 111:14925-14931, 2007.

[14] Bard, A.J., Faulkner, L.R., Leddy, J., and Zoski, C.G. Electrochemical methods: fundamentals and applications, second ed., *Wiley*, New York, 1980.